





# Characterising the turbulent multiphase halos with periodic box simulations

Rajsekhar Mohapatra <sup>1</sup>★, Mrinal Jetti <sup>2</sup>†, Prateek Sharma <sup>3</sup>‡ and Christoph Federrath <sup>1,4</sup>§

<sup>1</sup>Research School of Astronomy and Astrophysics, Australian National University, Canberra, ACT 2611, Australia

<sup>2</sup>Department of Aerospace Engineering, Indian Institute Of Technology, Chennai, Tamil Nadu 600036, India

<sup>3</sup>Department of Physics, Indian Institute of Science, Bangalore, KA 560012, India

<sup>4</sup>Australian Research Council Centre of Excellence in All Sky Astrophysics (ASTRO3D), Canberra, ACT 2611, Australia

Accepted XXX. Received YYY; in original form ZZZ

## ABSTRACT

Turbulence in the intracluster medium (ICM) is driven by active galactic nuclei (AGNs) jets, by mergers, and in the wakes of infalling galaxies. It not only governs gas motion but also plays a key role in the ICM thermodynamics. Turbulence can help seed thermal instability by generating density fluctuations, and mix the hot and cold phases together to produce intermediate temperature gas ( $10^4$ – $10^7$  K) with short cooling times. We conduct high resolution ( $384^3$ – $768^3$  resolution elements) idealised simulations of the multiphase ICM and study the effects of turbulence strength, characterised by  $f_{\text{turb}}$  (0.001–1.0), the ratio of turbulent forcing power to the net radiative cooling rate. We analyse density and temperature distribution, amplitude and nature of gas perturbations, and probability of transitions across the temperature phases. We also study the effects of mass and volume weighted thermal heating and weak ICM magnetic fields. For low  $f_{\text{turb}}$ , the gas is distribution is bimodal between the hot and cold phases. The mixing between different phases becomes more efficient with increasing  $f_{\text{turb}}$ , producing larger amounts of the intermediate temperature gas. Strong turbulence ( $f_{\text{turb}} \geq 0.5$ ) generates larger density fluctuations and faster cooling, The rms logarithmic pressure fluctuation scaling with Mach number  $\sigma_{\ln \bar{p}}^2 \approx \ln(1 + b^2 \gamma^2 \mathcal{M}^4)$  is unaffected by thermal instability and is the same as in hydro turbulence. In contrast, the density fluctuations characterised by  $\sigma_s^2$  are much larger, especially for  $\mathcal{M} \lesssim 0.5$ . In magnetohydrodynamic runs, magnetic fields provide significant pressure support in the cold phase but do not have any strong effects on the diffuse gas distribution, and nature and amplitude of fluctuations.

**Key words:** methods: numerical – hydrodynamics – magnetohydrodynamics – turbulence – galaxies:halos – galaxies: clusters: intracluster medium

## 1 INTRODUCTION

An interplay between different phases is seen in many different terrestrial and astrophysical systems across a vast range of scales. This includes interactions between water vapour and air in the earth’s atmosphere (Aronovitz & Nelson 1984; Pal et al. 2016), the interface between hot and cold air in combustion (Bray & Cant 1991), solar corona mass ejections, loops, and coronal rain (Foullon et al. 2011, 2013; Antolin 2020), warm and hot phases of the interstellar medium (ISM) (Begelman & Fabian 1990; Slavin et al. 1993; Wolfire et al. 1995a; Vázquez-Semadeni et al. 2000; Audit & Hennebelle 2005; Hennebelle & Audit 2007; Glover et al. 2010), neutral molecular/atomic, nebular and hot X-ray emitting regions in the Milky Way’s wind (Fox et al. 2015; Bordoloi et al. 2017; Di Teodoro et al. 2020), the circumgalactic medium (CGM) (Wolfire et al. 1995b; Tumlinson et al. 2011; Werk et al. 2014; Tumlinson et al. 2017; Marchal et al. 2021) and the intracluster medium (ICM) (Tremblay et al.

2018; Gendron-Marsolais et al. 2018; Olivares et al. 2019; Boselli et al. 2019; Rose et al. 2019; Vantygghem et al. 2019, 2021). The mixing between these different phases is often governed by turbulent gas motions. Understanding the nature and properties of these phases and the interactions between them is crucial for physical understanding.

In this study, we have focused on turbulence in the multiphase ICM of cool core clusters, where the ambient medium is made up of a hot X-ray emitting phase ( $\sim 10^7$ – $10^8$  K) with cooler atomic clouds/filaments, at  $\sim 10^4$  K often traced by H $\alpha$  emission, embedded in between. We also observe molecular gas at  $\sim 10$  K, traced by CO (Edge 2001), co-spatial with the atomic clouds (Hu 1992; Conselice et al. 2001; McDonald et al. 2012; Werner et al. 2013, 2014; Tremblay et al. 2018). Turbulence in the intracluster medium is primarily driven by AGN jets and by mergers (Balbus & Soker 1990; Churazov et al. 2002, 2003; Omma et al. 2004; Nelson et al. 2012). In addition to mixing the hot and cold phases, turbulence also plays several other important roles in the ICM, such as heating and seeding density fluctuations.

Since the ambient ICM is hot, ionised and optically thin, it emits free-free bremsstrahlung and cools radiatively (see Böhringer & Werner 2010 for a review), and the cooling time decreases with

★ E-mail: rajsekhar.mohapatra@anu.edu.au (RM)

† E-mail: mrinaljetti@gmail.com (MJ)

‡ E-mail: prateek@iisc.ac.in (PS)

§ E-mail: christoph.federrath@anu.edu.au (CF)

increasing density. Thus, cooler and denser gas cools faster, and without any heating, the cool core is expected to undergo runaway cooling flow until it eventually forms molecular gas. Turbulence can heat the ambient medium via turbulent dissipation, thus increasing its cooling time and averting a cooling flow. Turbulent mixing can transfer the AGN feedback power dissipated in the hot phase to the cooler gas. In these cases, turbulence prevents runaway cooling.

Turbulence also seeds thermal instability, by generating density fluctuations in which the overdense regions cool faster. It can also mix the cold and hot phase gas together to make intermediate temperature gas ( $10^5 - 10^6$  K), which then cools rapidly into the cold phase. Turbulence affects the density and temperature distribution of the ICM gas. It is therefore important to accurately quantify the role of turbulence in the ICM.

Observational studies have helped constrain the temperature distribution of the hot and intermediate phase gas, in addition to the cooler phases mentioned above. [Bregman et al. \(2006a\)](#) have noted a lack of intermediate temperature gas at around  $10^{5.5}$  K, which is traced by Ovi. [Anderson & Sunyaev \(2016\)](#) have looked at the far-UV forbidden lines Fexxi and Fexix which roughly trace gas around  $10^{6.5-10^7}$  K. In general, the flux in the lowest X-ray and far UV temperatures is much lower than predicted by the cooling-flow models, as summarised in [Peterson & Fabian \(2006\)](#). The soft X-ray filaments are also known to be multiphase and are associated with H $\alpha$  emission ([Sparks et al. 2004](#); [Fabian et al. 2006](#)).

Many recent observational studies have used different methods to estimate turbulent velocities in the ICM, summarised in the review by [Simionescu et al. \(2019\)](#). The Hitomi space telescope ([Hitomi Collaboration 2016](#)) directly measured velocities of the hot-phase gas by resolving the line-broadening of Fexxv and Fexxvi lines and revealed low levels of turbulence (roughly 4 percent of the thermal pressure) in the central regions of the Perseus cluster. XRISM<sup>1</sup>, the successor to Hitomi is expected to be launched in 2022, providing us a direct measurement of turbulent velocity in the volume-filling hot phase of the ICM for a sample of clusters. [Zhuravleva et al. \(2014a, 2018\)](#) have measured X-ray surface brightness fluctuations of several nearby galaxy clusters and used it to indirectly infer velocities of the hot phase. [Khatri & Gaspari \(2016\)](#) have used Planck data of the Coma cluster to calculate pressure fluctuations using the thermal Sunyaev-Zeldovich effect ([Zeldovich & Sunyaev 1969](#); [Sunyaev & Zeldovich 1970](#)) (tSZ), which can be further used to calculate turbulent pressure fluctuations and velocities. More recently, [Li et al. \(2020\)](#) have used velocity measurements of gas in the cold ( $10^4$  K) and molecular (10 K) phases in the ICM of nearby clusters to construct velocity structure functions. These structure functions are steeper than expected from Kolmogorov turbulence theory ([Kolmogorov 1941](#)).

Many recent numerical studies have also approached this problem, at many different scales. [Ji et al. \(2019\)](#); [Fielding et al. \(2020\)](#); [Tan et al. \(2021\)](#) have zoomed into the mixing layers between hot and cold phases. [Armillotta et al. \(2016\)](#); [Banda-Barragán et al. \(2016\)](#); [Gronke & Oh \(2018\)](#); [Kanjilal et al. \(2021\)](#) and many others have looked at the survival of a cold cloud moving through a hot ambient medium. [Banerjee & Sharma \(2014\)](#); [Mohapatra & Sharma \(2019\)](#); [Grete et al. \(2020\)](#) have looked at simulations of turbulence with thermal instability in idealised local box simulations. Studies such as [Hillel & Soker \(2020\)](#); [Wang et al. \(2021\)](#) have conducted isolated galaxy cluster simulations and looked at the turbulent velocity structure functions of hot and cold phases. Using similar setups, [Wittor](#)

& [Gaspari \(2020\)](#) have looked at the relation between enstrophy, a proxy of turbulence and its sinks and sources. At even larger scales, [Nelson et al. \(2020\)](#) have zoomed into individual halos in cosmological simulations and studied the multiphase environment within them.

While most of the small-scale simulations (mixing layer and wind-cloud) capture the interactions between the different phases in detail, they generally lack a more global perspective, such as the distribution of gas among different phases and statistical properties of the hot phase. Large cluster-scale and cosmological zoom-in simulations have enough samples of these multiphase interactions to get reliable statistics, but they often lack the resolution to resolve mixing layers and turbulence in much detail. Variable resolution in these simulations (due to adaptive mesh refinement, moving meshes or smoothed particle hydrodynamics) also makes it difficult to study turbulent statistics due to the spatio-temporal variation of numerical viscosity ([Fromang & Papaloizou 2007](#); [Mitran 2009](#); [Creasey et al. 2011](#); [Bauer & Springel 2012](#)). It is also difficult to do controlled parameter studies in these global simulations.

Local idealised box simulations are well-placed to tackle these issues - the boxes are large enough to perform these statistical studies, the setups are flexible and numerically cheap to do controlled parameter scans, while still having enough resolution to study turbulence through structure functions, power spectra and scaling relations between density, pressure and velocity fluctuations. Among the recent studies of the multiphase turbulent ICM in these setups, [Banerjee & Sharma \(2014\)](#); [Mohapatra & Sharma \(2019\)](#) lack the resolution to study turbulent structure functions. They also use a relatively high cutoff for the cold-phase gas ( $10^6$  K), which reduces the scale separation between different phases and may promote enhanced mixing between them. [Grete et al. \(2020\)](#) performed high-resolution magnetohydrodynamic (MHD) simulations, but they used an idealised cooling function (with proxies for free-free and linear cooling functions) to match the turbulent heating rate. These simulations, however, may have weaker cooling, since [Mohapatra & Sharma \(2019\)](#) using a similar setup showed that matching the turbulent heating rate to a realistic cooling rate would result in supersonic gas motions. The hot ICM is known to be subsonic. Hence to understand the interaction between the different phases and their kinematics, we need to conduct high-resolution simulations (with converged slopes of structure functions) with accurate implementation of cooling in the hot-phase gas, while maintaining the scale separation between the phases (by choosing lower cooling cutoffs, at  $10^4$  K).

Here we conduct a set of local simulations of homogeneous isotropic turbulence with radiative cooling in a box of size 40 kpc. We mainly scan the parameter space of the turbulent heating fraction parameter  $f_{\text{turb}}$  (defined in the next section). We also compare between our simulations with and without magnetic fields and two different types of idealised thermal heating models (namely heating  $\propto \rho^1$  &  $\propto \rho^0$ ). In this study, we introduce our model and setup. We mainly discuss the distributions of various thermodynamic properties (gas density, pressure and temperature) of the ICM. We study the statistical relations between these properties, such as the scaling relation between density and pressure fluctuations ( $\sigma_s$  and  $\sigma_{\ln \bar{p}}$ ) and the rms Mach number ( $M$ ). We analyse the phase diagrams of the ICM gas and the probability of transition between the different phases (using tracer particles), and how they vary with our parameters. In a companion study ([Mohapatra et al. 2021a](#)), we compare between the kinematics of the cold and hot phases of the gas in these simulations using velocity structure functions.

This paper is organised as follows. In section 2, we introduce our setup and numerical methods. In section 3, we present the key results

<sup>1</sup> <https://heasarc.gsfc.nasa.gov/docs/xrism>

of our simulations and discuss their implications. We discuss our caveats and future prospects in section 4. We finally summarise and conclude the study in section 5.

## 2 METHODS

### 2.1 Model equations

We model the ICM as a fluid using the compressible MHD equations and the ideal gas equation of state. We solve the following equations:

$$\frac{\partial \rho}{\partial t} + \nabla \cdot (\rho \mathbf{v}) = 0, \quad (1a)$$

$$\frac{\partial (\rho \mathbf{v})}{\partial t} + \nabla \cdot (\rho \mathbf{v} \otimes \mathbf{v} + P^* \mathbf{I} - \mathbf{B} \otimes \mathbf{B}) = \rho \mathbf{F}, \quad (1b)$$

$$\frac{\partial E}{\partial t} + \nabla \cdot ((E + P^*) \mathbf{v} - (\mathbf{B} \cdot \mathbf{v}) \mathbf{B}) = \rho \mathbf{F} \cdot \mathbf{v} + Q - \mathcal{L}, \quad (1c)$$

$$\frac{\partial \mathbf{B}}{\partial t} - \nabla \times (\mathbf{v} \times \mathbf{B}) = 0, \quad (1d)$$

$$P^* = P + \frac{\mathbf{B} \cdot \mathbf{B}}{2}, \quad (1e)$$

$$E = \frac{\rho \mathbf{v} \cdot \mathbf{v}}{2} + \frac{P}{\gamma - 1} + \frac{\mathbf{B} \cdot \mathbf{B}}{2}, \quad (1f)$$

where  $\rho$  is the gas mass density,  $\mathbf{v}$  is the velocity,  $\mathbf{B}$  is the magnetic field,  $P = \rho k_B T / (\mu m_p)$  is the thermal pressure,  $\mathbf{F}$  is the turbulent force per unit mass that we apply,  $E$  is the total energy density,  $\mu$  is the mean molecular mass,  $m_p$  is the proton mass,  $k_B$  is the Boltzmann constant,  $T$  is the temperature,  $Q(t)$  and  $\mathcal{L}(\rho, T)$  are the thermal heating and cooling rate densities respectively, and  $\gamma = 5/3$  is the adiabatic index. The cooling rate density  $\mathcal{L}$  is given by

$$\mathcal{L} = n_e n_i \Lambda(T), \quad (2)$$

where  $\Lambda(T)$  is the temperature-dependent cooling function of [Sutherland & Dopita \(1993\)](#) corresponding to  $Z_{\odot}/3$  solar metallicity, and  $n_e$  and  $n_i$  are electron and ion number densities, respectively. Viscosity and thermal conduction are not included explicitly.

### 2.2 Numerical methods

We evolve equations 1a to 1f using the HLL5R Riemann solver ([Bouchut et al. 2007, 2010](#); [Waagan et al. 2011](#)) in a modified version of the FLASH code ([Fryxell et al. 2000](#); [Dubey et al. 2008](#)), version 4. We use the MUSCL-Hancock scheme ([Van Leer 1984](#); [Waagan 2009](#)) for time integration and a second-order reconstruction method that uses primitive variables and ensures positivity of density and internal energy. For magnetic fields, we use divergence cleaning in the form of the parabolic cleaning method of [Marder \(1987\)](#). For most of our runs, we solve the hydrodynamic (HD) equations (by setting  $\mathbf{B} = 0$ ), but we also have two runs with MHD for comparison. We use a uniformly spaced 3D Cartesian grid with  $L_x = L_y = L_z = L = 40$  kpc, where  $L$  is the box size, with a default resolution of  $384^3$ . This gives us an effective spatial resolution of roughly 100 pc. Our boundary conditions are periodic. We have tested the code for convergence by doubling the resolution to  $768^3$ .

#### 2.2.1 Turbulent forcing

We follow a spectral forcing method using the stochastic Ornstein-Uhlenbeck (OU) process to model the turbulent acceleration field  $\mathbf{F}$  with a finite autocorrelation time-scale  $t_{\text{turb}}$  ([Eswaran & Pope 1988](#);

[Schmidt et al. 2006](#); [Federrath et al. 2010](#)), which is fixed to 260 Myr across all our simulations. We only excite the large-scale modes with  $1 \leq |\mathbf{k}|L/2\pi \leq 3$ . The power is a parabolic function of  $k$  and peaks at  $k = 2$  (we have dropped the wavenumber unit  $2\pi/L$  for simplicity). For scales smaller than these injection scales ( $k > 3$ ), turbulence develops self consistently. We make sure that the driving field is solenoidal by removing the divergent component (component along  $\mathbf{k}$ ). For more details of the forcing method, refer to section 2.1 of [Federrath et al. \(2010\)](#). We use the same acceleration field (with the same random seed) for all our simulations, except that we scale the amplitude dynamically to impose global thermal balance, which we describe in the following section.

#### 2.2.2 Global energy balance

We maintain global energy balance in all our simulations, which is motivated by the lack of cooling flows in observations. We achieve this by controlling the amplitudes of thermal heating rate  $Q$  and the turbulent energy injection rate. We introduce a parameter  $f_{\text{turb}}$ , which is the ratio of the turbulent energy injection rate to the radiative cooling rate. We impose the following condition at every time step:

$$\int \rho \mathbf{F} \cdot \mathbf{v} dV = f_{\text{turb}} \int \mathcal{L} dV. \quad (3)$$

The remaining energy loss is compensated by adding heat throughout the box. We follow two different methods - distributing this heat uniformly per mass and uniformly per volume. Mathematically, these are given by

$$Q_{\text{mw}}(\mathbf{x}, t) = \rho(\mathbf{x}, t) (1 - f_{\text{turb}}) \frac{\int \mathcal{L} dV}{\int \rho dV}, \quad (4a)$$

$$Q_{\text{vw}}(\mathbf{x}, t) = (1 - f_{\text{turb}}) \frac{\int \mathcal{L} dV}{\int dV}. \quad (4b)$$

Although both of these thermal heating methods are idealised,  $Q_{\text{mw}}$  is motivated by the several gas-density dependent heating processes, such as heating by photons and cosmic rays. Similarly,  $Q_{\text{vw}}$  represents the processes that deposit thermal energy in the hot volume-filling phase, such as AGN jets feeding buoyant bubbles, heating by mixing ([Banerjee & Sharma 2014](#)). We choose  $Q = Q_{\text{mw}}$  for most of our runs, but we also compare between these two implementations in section 3.6.1.

#### 2.2.3 Cooling cutoff

Since we do not consider gravity in this setup, thermally unstable regions of gas can separate out from the hot phase and collapse to small scales ([Field 1965](#); [Koyama & Inutsuka 2004](#); [Sharma et al. 2010](#)). Multiphase gas is prevented with gravity if the background  $t_{\text{cool}}/t_{\text{ff}} \gtrsim 10$  ([McCourt et al. 2012](#); [Choudhury & Sharma 2016](#)), where  $t_{\text{cool}}$  and  $t_{\text{ff}}$  are the cooling time and the free-fall time of the gas, respectively. In order to prevent the gas from cooling to very low temperatures, we set the cooling function to zero below a temperature  $T_{\text{cutoff}}$ . Assuming that the cooling gas goes not fragment and conserves its mass and reaches pressure equilibrium with the hot phase, the scale of the smallest clouds scales as  $T_{\text{cutoff}}^{1/3}$ . In addition to the temperature floor, we also impose a cooling pressure floor at roughly  $P_0/600$ , where  $P_0$  is the initial pressure, for additional numerical stability and to prevent negative pressure. Thus, the cooling function takes the form

$$\mathcal{L} = n_e n_i \Lambda(T) \mathcal{H}(T - T_{\text{cutoff}}) \mathcal{H}(P - P_0/600), \quad (5)$$

where  $\mathcal{H}$  is the Heaviside function. We set  $T_{\text{cutoff}} = 10^4$  K for all of our simulations, which is also the lower temperature limit of the cooling table that we use (Sutherland & Dopita 1993). This choice is reasonable, since one would also need additional physics to model gas cooling below  $10^4$  K, such as accurate modelling of different species and chemical networks, and heating due to interstellar background radiation and cosmic rays. Moreover, even higher resolution would be needed to sufficiently resolve the densest gas.

#### 2.2.4 Relevant timescales

Some important timescales of the system are the cooling time ( $t_{\text{cool}}$ ), thermal instability time scale  $t_{\text{TI}}$ , sound crossing time ( $t_{\text{cs}}$ ) and turbulent mixing time ( $t_{\text{mix}}$ ). They are given by

$$t_{\text{cool}} = \frac{E_{\text{int}}}{\mathcal{L}} = \frac{P}{(\gamma - 1)n_e n_i \Lambda(T)}, \quad (6a)$$

$$t_{\text{TI}} = \frac{\gamma t_{\text{cool}}}{2 - d \ln \Lambda / d \ln T - \alpha}, \quad (6b)$$

$$t_{\text{cs}} = \frac{L}{\sqrt{\frac{\gamma k_B T}{\mu m_p}}}, \text{ and} \quad (6c)$$

$$t_{\text{mix}} = \frac{L_{\text{inj}}}{v} \approx \frac{L}{2v}, \quad (6d)$$

where  $Q \propto \rho^\alpha$ ,  $\alpha = 1$  for  $Q_{\text{mw}}$  and  $\alpha = 0$  for  $Q_{\text{vw}}$  and  $v$  is the rms velocity. For the gas in the hot phase ( $T > 10^7$  K),  $\Lambda(T) \propto T^{1/2}$ , so  $t_{\text{TI}} \approx 3t_{\text{cool}}$  for mass-weighted heating and  $t_{\text{TI}} \approx t_{\text{cool}}$  for volume-weighted heating. See appendix of Sharma et al. (2010) for a derivation of  $t_{\text{TI}}$  using linear stability analysis.

#### 2.2.5 Sub-cycling for cooling

For gas in the intermediate phase ( $2 \times 10^4 - 10^6$  K),  $t_{\text{cool}}$  can be very short where  $\Lambda(T)$  peaks ( $\approx 10^{5.5}$  K). For an isobaric collapse,  $n_e, n_i \propto 1/T$ , but since the hot-phase gas is more volume-filling,  $t_{\text{cool}}$  is short only in small volume with high density and low temperature. Thus, it is numerically expensive to evolve the entire simulation domain at small time-steps set by the global minimum  $t_{\text{cool}}$  (given by  $t_{\text{cool, min}}$ ). Hence, we evolve the internal energy with operator splitting in the short  $t_{\text{cool}}$  grid cells using smaller time steps, such that the internal energy is not changing by more than 1/8th per subcycle. The number of subcycles is dependent on the local  $t_{\text{cool}}$  at each cell, which can be different for different cells. We evolve the rest of the cells at a slightly longer Euler time step ( $dt_{\text{code}}$ ), such that it is always less than 5 times  $t_{\text{cool, min}}$  ( $dt_{\text{code}} = \min(5t_{\text{cool, min}}, dt_{\text{CFL}}$ ), where  $dt_{\text{CFL}}$  is the time step set by the Courant criterion). We have tested our code both with and without subcycling, and our results are not affected by it.

#### 2.2.6 Tracer particles

We introduce 1000 Lagrangian tracer particles distributed uniformly throughout the volume at  $t = 0$ . These tracers move around the simulation domain according to the velocity of the cell they are in. They track the local temperature, density and magnetic field, and the entire trajectory of these tracers is stored as a time-series for further analysis. These tracers do not have any back-reaction on the gas.

### 2.3 Initial conditions

We initialise the gas with a temperature  $T_0 = 4 \times 10^6$  K,  $n_e = 0.086 \text{ cm}^{-3}$ , which corresponds to a sound speed of 300 km/s. The

gas has  $t_{\text{cool}} \sim 19$  Myr,  $t_{\text{TI}} \sim 57$  Myr and  $t_{\text{cs}} \approx 64$  Myr across the whole box. Since initially the gas motion is subsonic,  $t_{\text{mix}} > t_{\text{cs}} > t_{\text{TI}}$ . Thus, the gas is thermally unstable and forms multi-phase gas. Note that we start with gas temperatures somewhat lower than typical ICM temperatures of  $1-2 \times 10^7$  K. We choose these thermally unstable regions so that we can generate multiphase gas and study the interactions between the hot and cold phases. This setup can be directly compared with the inner regions of cool core clusters and not the whole ICM. After multi-phase gas condensation, the heat lost via cooling heats the ambient hot phase gas to typical ICM temperatures in the steady state (since we impose global energy balance). In reality, the hot phase temperature is set by the depth of the gravitational potential well but we do not model this in our simulations.

For our MHD runs, we set the initial magnetic field with equal mean and rms components, in the absence of strong observational constraints on the field geometry. The mean field is set in the  $z$  direction. The rms component is set as a power law, taking the form  $B_k \propto k^{1.25}$ , for  $2 \leq k \leq 20$  to model small-scale dynamo growth motivated by the Kazantsev spectrum (Kazantsev 1968). The initial plasma beta  $\beta$  (ratio of thermal to magnetic pressure) is 100.

### 2.4 List of Simulation models

We have conducted 10 simulations, mainly scanning the parameter space of  $f_{\text{turb}}$ , which are listed in table 1 along with some relevant simulation parameters. The run labels indicate the value of  $f_{\text{turb}}$ . We label the run **f0.10** as our **fiducial** run. Most of these runs use HD equations unless indicated in the label. Similarly, the default resolution is  $384^3$  and the default model for thermal heating is  $Q_{\text{mw}}$  ( $\propto \rho$ ; see section 2.2.2), unless indicated in the run label. For studying the effects of MHD, we introduce magnetic fields to the fiducial run. Similarly to study differences (if any) between the different models of thermal heating, we use volume-weighted thermal heating in f0.10vw. In order to check convergence of our results, we have higher resolution runs (labelled ‘HR’, with  $768^3$  resolution elements) for the fiducial, MHD and vw runs. We have run most of our simulations till 1.302 Gyr, and only two high-resolution simulations (f0.10HR and f0.10magHR) till 1.003 Gyr since they are numerically expensive.

## 3 RESULTS AND DISCUSSION

In this section, we present our results and discuss their possible interpretations. We first focus on the effects of different levels of turbulence (by varying  $f_{\text{turb}}$ ) and then describe the effects of higher resolution, MHD and volume-weighted thermal heating.

### 3.1 2D projection maps

In fig. 1 we show the line-of-sight (LOS) projections of density (column density  $\Sigma_{\text{LOS}}$ , first column), mass-weighted temperature ( $T_{\text{LOS}}$ , second column), and net emission from cold phase gas ( $n_e n_i \Lambda(T)_{\text{LOS}}$ , for  $10^4 \text{ K} < T < 2 \times 10^4 \text{ K}$ , third column) for three representative simulations – our fiducial run (f0.10, second row) and the two extreme runs with almost no-turbulent heating (f0.001, first row) and fully turbulent heating (f1.00, third row). We choose the  $x$ -direction as our LOS. In the second column, we also show the LOS-projection of the velocity field perpendicular to the LOS, as cyan arrows (dark-cyan for f0.001). All the colorbars are in the log-scale.

In the first column, for the f0.001 run, we observe that without turbulence, the gas is distributed bimodally into small dense clouds

**Table 1.** Simulation parameters for different runs.

Label (1)	Resolution (2)	$f_{\text{turb}}$ (3)	Thermal heating (4)	$\mathcal{M}_{\text{hot}}$ (5)	$v$ (km/s) (6)	Magnetic fields (7)	$t_{\text{end}}$ (Gyr) (8)
f0.001	384 <sup>3</sup>	0.001	mass-weighted	0.087 ± 0.002	110 ± 5	N	2.604
f0.04	384 <sup>3</sup>	0.04	mass-weighted	0.43 ± 0.01	320 ± 30	N	1.302
f0.10 (fiducial)	384 <sup>3</sup>	0.10	mass-weighted	0.55 ± 0.03	350 ± 40	N	1.302
f0.10HR	768 <sup>3</sup>	0.10	mass-weighted	0.91 ± 0.05	370 ± 40	N	1.003
f0.50	384 <sup>3</sup>	0.50	mass-weighted	1.55 ± 0.08	400 ± 60	N	1.302
f1.00	384 <sup>3</sup>	1.00	N	1.64 ± 0.07	410 ± 80	N	1.302
f0.10mag	384 <sup>3</sup>	0.10	mass-weighted	0.39 ± 0.02	330 ± 40	Y	1.302
f0.10magHR	768 <sup>3</sup>	0.10	mass-weighted	0.59 ± 0.05	330 ± 40	Y	1.003
f0.10vw	384 <sup>3</sup>	0.10	volume-weighted	0.19 ± 0.01	340 ± 20	N	1.302
f0.10vwHR	768 <sup>3</sup>	0.10	volume-weighted	0.23 ± 0.01	370 ± 30	N	1.003

Notes: Column 1 shows the simulation label. The number following ‘f’ denotes  $f_{\text{turb}}$ , also shown in column 3, which is the ratio of turbulent energy input rate to the radiative cooling rate, described in eq. (3). In column 2 we list the resolution of the simulations. The default resolution of all the runs is 384<sup>3</sup> cells, unless indicated by the label ‘HR’ for 768<sup>3</sup> cells. Column 4 lists the type of thermal heating (volume-weighted or mass-weighted) implemented in the simulations (see eq. 4a and 4b) which is by default set to mass-weighted, unless indicated in the simulation labels as ‘vw’. In column 5, we denote the steady state rms Mach number ( $\mathcal{M}_{\text{hot}}$ ) of the hot-phase gas (see section 3.3.5 for its description). In column 6, we show the steady state rms velocity ( $v$ ) in km/s and in column 7, we denote whether magnetic fields are switched on. Runs with magnetic fields are labelled by ‘mag’. Finally, in column 8, we show the end time of a simulation in Gyr.

and large regions with almost no gas. They have gas densities around an order of magnitude larger and smaller than the mean density, respectively. In the fiducial run (second row), we observe a lot more gas at intermediate densities (orange-light purple colour). The size of the dense clouds is larger, and their densities are somewhat smaller. There are also less empty regions. In the third row, for the f1.00 run, the gas densities are even closer to the mean density, with the extreme density regions almost disappearing. Thus increasing turbulent heating fraction leads to increased mixing between the dense clouds and the ambient medium, which smoothens the density distribution.

In the second column, for the no-turbulence run (f0.001), we notice that the lower temperature regions correspond to the dense clouds in the first column, which is expected. The low density regions also correspond to the hot phase, which is at a fairly high temperature ( $T \geq 10^{7.5}$  K). For the fiducial run, we observe more gas at intermediate temperatures (between  $2 \times 10^4$ – $10^6$  K). The hot phase is also at a slightly smaller temperature ( $\sim 10^7$  K). For the f1.00 run, most of the projected temperature is close to or below the cooling cutoff at  $10^4$  K. We do not see a very clear hot phase, as there is not much gas with  $T > 10^6$  K. For all of these runs, we do not observe any obvious correlation between the amplitude of projected velocity and the temperature/phase of the gas.

In the third column, we show the net emission measure from gas in the cold phase ( $10^4$  K  $< T < 2 \times 10^4$  K), which is a proxy for  $H\alpha$  emitting regions in the CGM/ICM. In the absence of turbulence, we observe emission coming from many small dense and cool clouds. With increasing turbulence, this emission gets smeared out. The magnitude of emission decreases but it covers many more sightlines along the LOS due to turbulent mixing. The emission strength for f1.00 run is also smaller because a lot of gas is cooled (below  $10^4$  K) due to strong turbulent rarefaction (see second column of third row), and such gas is assumed to be non-radiating.

However, it is important to note that the size of the cold clouds could be much smaller and their area covering fraction much larger in reality (and in higher resolution simulations), since we do not resolve the cooling length ( $\ell_{\text{cool}} = c_s t_{\text{cool}}$ ) in our simulations. The

scale  $\ell_{\text{cool}}$  reaches a minimum of  $\approx 0.1$  pc for the cold fast-cooling regions, much smaller than our resolution of  $\approx 100$  pc. Later we have discussed the convergence of our results with respect to resolution (section 3.6.3). The appearance of smaller scale features with increasing resolution is expected as finer scales emerge with increasing Reynolds numbers.

These results have implications for the observational probes of the CGM. The size and covering fraction of these cold clouds could be used as a crude estimate of the level of turbulence in these systems (Tremblay et al. 2018; Olivares et al. 2019; Vantghem et al. 2021).

### 3.2 Evolution of density perturbations and energy

In the upper panel of fig. 2, we show the net cold gas mass fraction (fraction of gas with  $T < 2 \times 10^4$  K) as a function of time for our five runs with different  $f_{\text{turb}}$ . In the middle panel, we show the time evolution of the thermal energy ( $E_{\text{therm}}$ ) and in the third panel we show the volume-weighted Mach number ( $\mathcal{M}$ ).

Our simulations start with the gas at  $4 \times 10^6$  K (no cold gas). Turbulence generates density fluctuations in the gas. These regions are thermally unstable since  $t_{\text{TI}} < t_{\text{mix}}$  ( $t_{\text{cool}} = 19$  Myr,  $t_{\text{TI}} \sim 57$  Myr,  $t_{\text{mix}} = 92$  Myr). The over-dense regions cool all the way down to  $10^4$  K (till  $T_{\text{cutoff}}$ ). We introduce a timescale  $t_{\text{multiphase}}$  which corresponds to the onset of cold gas in these simulations, defined as the time when  $m_{\text{cold}}/m_{\text{tot}} > 0.1$ . This timescale  $t_{\text{multiphase}}$  is shorter for larger  $f_{\text{turb}}$  runs because they seed larger over-densities with shorter cooling times.

In steady state, the value of  $m_{\text{cold}}/m_{\text{tot}}$  (upper panel) first decreases with increasing  $f_{\text{turb}}$  till f0.10 and then increases. This can be attributed to the effects of turbulent mixing and turbulent rarefaction. For  $f_{\text{turb}} \lesssim 0.1$ , with increasing  $f_{\text{turb}}$ , turbulent mixing between gas at the cooling cutoff and the hot phase gas pushes more and more of the cold gas to the intermediate phase (towards  $\sqrt{T_{\text{hot}} T_{\text{cutoff}}}$  which decreases the mass fraction of cold gas with increasing  $f_{\text{turb}}$ . But for  $f_{\text{turb}} \gtrsim 0.1$ , an increasing fraction of radiatively lost thermal energy

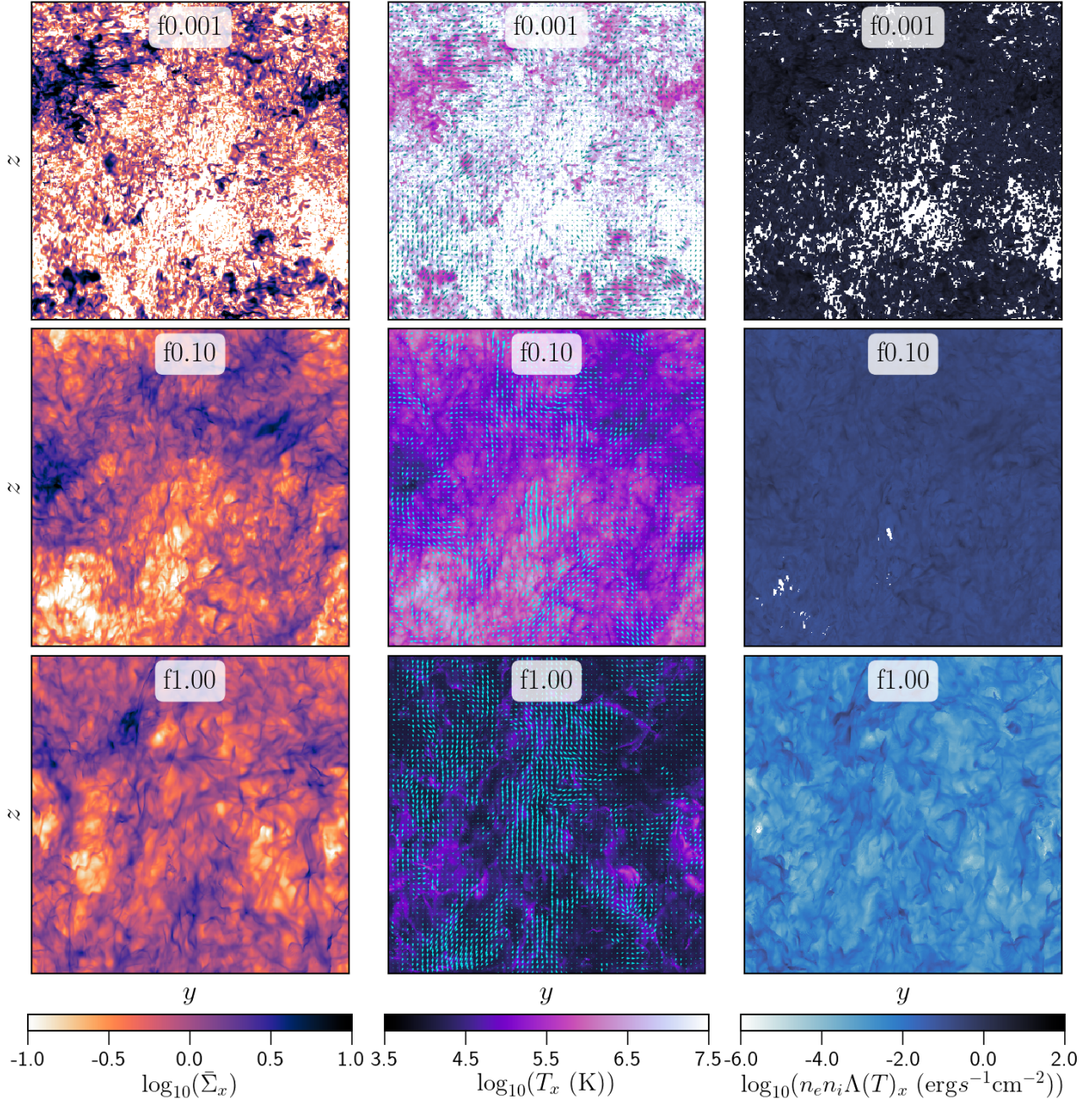


**Figure 1.** First column: snapshots of normalised density projected along the  $x$  direction at  $t = 1.042$  Gyr for three representative simulations: f0.001, f0.10 and f1.00. Second column: mass-weighted projections of temperature at this snapshot along the  $x$  direction for these runs. The cyan (dark-cyan for f0.001) arrows show the projected velocity field in the  $yz$  plane. Third column: net emission from cold gas ( $T < 2 \times 10^4$  K) along the  $x$  direction. All colorbars are in log scale, and are shown at the bottom of each column. Note that the area covering fraction of cold gas is larger for higher turbulence, even though the mass fraction is larger for the f0.001 run as compared to the f1.00 run (see the top panel of fig. 2). These colormaps are available in the cmasher package (van der Velden 2020).

is also supplied as kinetic energy because of the imposed global thermal balance, and this leads to supersonic turbulent velocities (see lower panel). This strong turbulence cools the hot phase gas (through supersonic rarefactions), which leads to an increase in  $m_{\text{cold}}/m_{\text{tot}}$  with increasing  $f_{\text{turb}}$ .

Since the simulations are in global energy balance, the lost  $E_{\text{therm}}$  is added back into the system in the form of turbulent kinetic energy ( $E_{\text{kin}}$ ,  $f_{\text{turb}}$  fraction) and thermal heat ( $1 - f_{\text{turb}}$  fraction). The steady state ( $t \gg t_{\text{multiphase}}$ ) value of  $E_{\text{therm}}$  decreases with increasing

$f_{\text{turb}}$ , and an increasing fraction of energy is retained as  $E_{\text{kin}}$ . With increasing  $f_{\text{turb}}$ , the effective conversion of thermal energy to  $E_{\text{kin}}$  also leads to increasing  $\mathcal{M}$ , as seen in the lower panel.

### 3.3 Probability distribution functions

In this section, we describe the probability distribution functions (PDFs) of various thermodynamic properties of our gas, and how they depend on the parameter  $f_{\text{turb}}$ . This analysis can help us un-

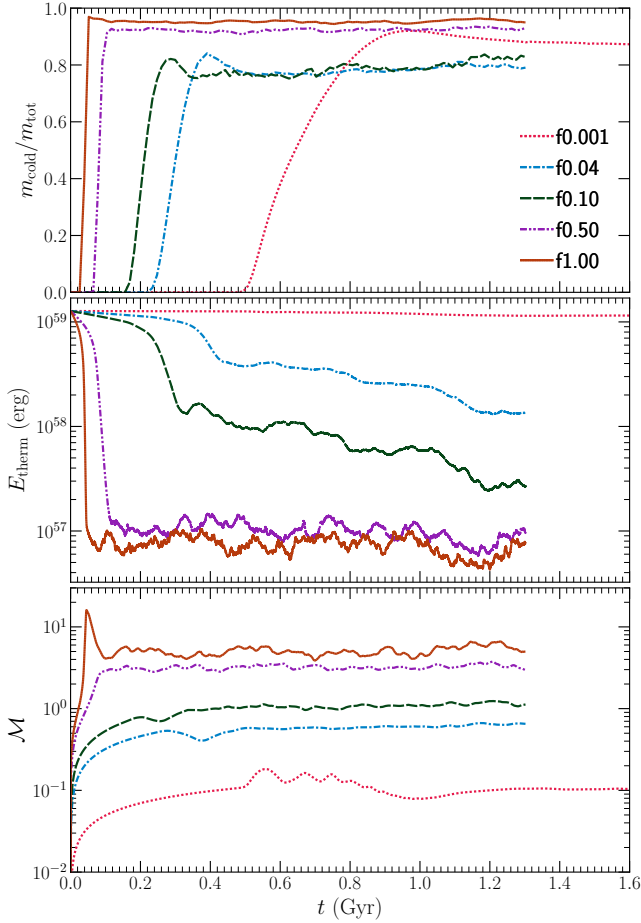


**Figure 2.** Time evolution of mass fraction of gas in the cold phase (first panel  $m_{\text{cold}}/m_{\text{tot}}$ ), thermal energy (second panel  $E_{\text{therm}}$ ), and volume-weighted rms Mach number (third panel  $\mathcal{M}$ ). Although  $E_{\text{therm}}$  drops initially for the runs with stronger turbulence, the total energy (including  $E_{\text{kin}}$ ) is approximately constant by construction. We have run the f0.001 run for longer time, since it reaches a steady state only around  $t = 1$  Gyr.

understand the observed CGM/ICM properties, such as the relative abundance/absence of intermediate temperature gas and how it depends on the strength of turbulence (Werk et al. 2014; Tumlinson et al. 2017) in the CGM and the ICM. They can also help us make predictions for future observations, such as quasar LOS studies of faint galaxies using the James Webb Space Telescope (JWST), emission from the hot phase gas using the Large Ultraviolet/Optical/Near Infrared Surveyor (LUVOIR<sup>2</sup>) and the Advanced Telescope for High ENergy Astrophysics (ATHENA<sup>3</sup>).

### 3.3.1 Mach number PDF

In fig. 3, we show the volume PDF of Mach number. The PDFs have two distinct peaks, where the low Mach number peak corresponds to the hot phase (which has larger sound speed) and the high Mach number peak corresponds to the cold phase. As expected, with increasing  $f_{\text{turb}}$ , both the peaks move towards larger Mach numbers

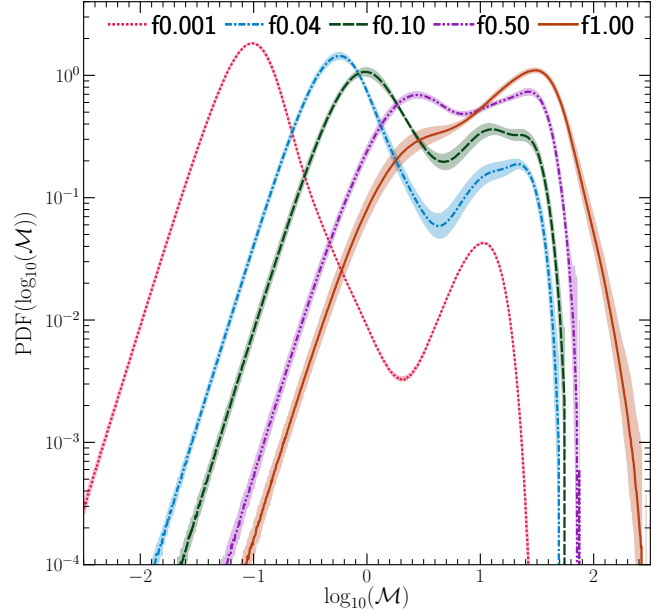


**Figure 3.** The volume PDF of the logarithm of Mach number of the gas for different  $f_{\text{turb}}$ , averaged over 400 Myr in steady state. The shaded regions around the lines indicate the temporal variation (standard deviation of  $\log_{10}(\text{PDF})$ ). The higher Mach number peak becomes more prominent with increasing  $f_{\text{turb}}$  due to higher turbulent velocity and cooler gas. The hot phase peak (lower Mach number) becomes supersonic due to increased turbulent forcing.

due to stronger turbulent driving. The two peaks come closer to each other, and there is more gas at intermediate Mach numbers, due to increased turbulent mixing. The amplitude of the cold phase peak increases by an order of magnitude, since turbulent diffusion smears out the cold dense regions so that they occupy more volume.

The rms velocity of the hot and cold phases is similar and the Mach number peaks essentially reflect the temperatures of the two dominant phases. The supersonic Mach number peak corresponding to the cold phase does not reflect the internal velocities within clouds but mostly their bulk motions.

The hot phase peak becomes supersonic for  $f_{\text{turb}} \gtrsim 0.5$ , which is inconsistent with the subsonic ICM (Hitomi Collaboration 2016). In Mohapatra & Sharma (2019), we used this argument to rule out turbulent dissipation to be the main source of heating the ICM, since it results in a larger turbulent to thermal pressure ratio compared to the observations by Hitomi (Table 1 shows that the mass-weighted thermal heating gives higher Mach numbers compared to the volume-weighted runs). However, the results from  $f_{\text{turb}} \gtrsim 0.5$  could be applicable to smaller halos such as the CGM, which we discuss further in the following subsections.

### 3.3.2 Temperature PDF

We show the volume PDFs of temperature for different  $f_{\text{turb}}$  runs in fig. 4. We observe two major peaks in most of the PDFs, one at  $T_{\text{cutoff}}$  corresponding to the cold phase and another between  $10^6$ – $10^8$  K at  $T_{\text{hot}}$ , corresponding to the hot phase. Only for the f1.00 run, there is no peak at  $T \gtrsim 10^6$  K. With increasing  $f_{\text{turb}}$ ,  $T_{\text{hot}}$  decreases, since a larger fraction of energy is deposited as turbulent energy rather than thermal. The volume of gas at intermediate temperatures also increases due to turbulent mixing between the hot and cold phases.

<sup>2</sup> <http://asd.gsfc.nasa.gov/luvoir/>

<sup>3</sup> <http://sci.esa.int/cosmic-vision/54517-athena/>

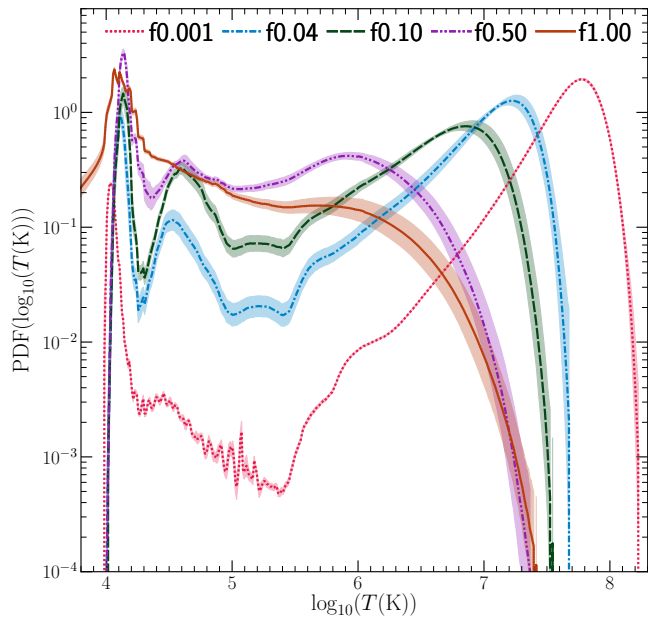


**Figure 4.** The volume PDF of the logarithm of temperature of the gas for different fractions of turbulent heating. The amount of gas in the intermediate phase increases with increasing  $f_{\text{turb}}$ . The hot phase is cooler for larger  $f_{\text{turb}}$  as turbulence mixes the hottest gas and cools it.

For  $f_{\text{turb}} = 0.04, 0.10$  runs, the bumps in the PDF trace features of the cooling curve, with a dip near the cooling peak ( $10^{5.5}$  K, where  $t_{\text{cool}}$  is short) and the bumps correspond to build-up of gas just below this peak. For the f1.00 run, we also see a lot of gas below  $T_{\text{cutoff}}$ . This gas cools due to rarefactions in supersonic turbulence.

The trends in the PDF with increasing  $f_{\text{turb}}$  are similar to the trends in temperature PDFs in Nelson et al. (2020) with decreasing halo mass (see their figure 6). Smaller halos are expected to have larger deviations from hydrostatic equilibrium, and thus a larger turbulent Mach number (Oppenheimer 2018). The f0.50 and f1.00 temperature PDFs are almost flat in intermediate-hot phase temperatures due to highly efficient turbulent mixing. They appear similar to the temperature PDFs in the multiphase wind-cloud simulations in Kanjilal et al. (2021) (see their figure 5).

The abundance of gas at these intermediate temperatures is traced by ions such as MgII ( $\sim 10^4$  K), CIV and SiIV ( $\sim 10^5$  K), NV and OVI ( $\sim 10^{5.5}$  K) (see fig. 6 of the review by Tumlinson et al. (2017)), which can be detected through their absorption features in the spectra of background quasars and also by emission from nearby bright sources. Since the amount of gas at intermediate temperatures strongly depends on  $f_{\text{turb}}$ , we can use the relative abundance of these ions to place constraints on the turbulent pressure fraction of the gas. Observations of galaxy clusters do not show strong, volume-filling emission in the far UV and soft X-ray bands, but rather find it to be confined to filamentary regions forming a boundary layer between the cold and hot phases (Bregman et al. 2006b; Werner et al. 2013; Anderson & Sunyaev 2018). These results favour a weak turbulent feedback (low  $f_{\text{turb}}$ ) scenario for the ICM.

### 3.3.3 Pressure PDF

In fig. 5, we show the volume-weighted PDF of thermal pressure normalised by the initial mean value. The shapes of these PDFs vary

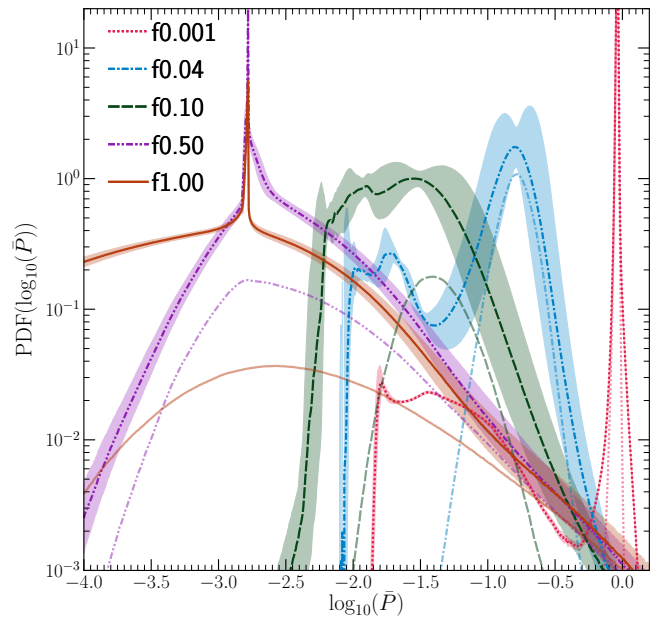


**Figure 5.** The volume-weighted PDF of the logarithm of pressure (normalised) for different fractions of turbulent heating, with shaded regions showing the  $1-\sigma$  error interval. The lighter colored lines show the pressure PDFs for the hot phase gas ( $T > 10^7$  K for  $f_{\text{turb}} \leq 0.10$  and  $T > 10^6$  K for  $f_{\text{turb}} > 0.10$ ). A low pressure tail develops for the supersonic/transonic cases (f0.50 and f1.00 runs). The pressure PDF is bimodal for weaker driving, as gas at intermediate temperatures cools isochorically rather than isobarically. For the hot phase PDFs, note that the ambient pressure is smaller for larger  $f_{\text{turb}}$ , which crudely mimics the CGM of different mass halos.

the most with varying  $f_{\text{turb}}$ . The low  $f_{\text{turb}}$  (f0.001, f0.04) runs show two peaks, where the low pressure peak corresponds to the cold phase. With increasing  $f_{\text{turb}}$ , turbulence broadens these peaks (width  $\propto \mathcal{M}^2$ , see Mohapatra & Sharma 2019; Mohapatra et al. 2021b). The mean thermal pressure ( $\langle P \rangle$ ) decreases with increasing  $f_{\text{turb}}$  because of predominant kinetic energy injection (also see second row of fig. 2). The peak at  $\log_{10} \bar{P} = -2.78$  in f0.50 and f1.00 runs corresponds to our cooling pressure floor (see eq. 5), so gas with  $P < P_{\text{cutoff}}$  is generated by turbulent supersonic rarefactions.

The pressure distribution of the hot phase is relevant for tSZ observations, which is a measure of the LOS integral of the hot phase electron pressure. Here we define the hot phase as  $T > 10^7$  K for  $f_{\text{turb}} \leq 0.10$  and  $T > 10^6$  K for  $f_{\text{turb}} > 0.10$ . This choice is reasonable since temperature PDFs of high  $f_{\text{turb}}$  runs are similar to smaller halos (intra-group medium and CGM) (see section 3.3.2), for which the hot phase is at  $10^6-10^7$  K.

The hot phase pressure PDFs for these runs are shown in fig. 5 as lighter colored lines. For  $f_{\text{turb}} \leq 0.10$ , the pressure distribution is log-normal and its peak lines up with the high-pressure peak. The f0.50 and f1.00 runs show extended high-pressure tails and the PDF spans over 4–5 orders of magnitude.

### 3.3.4 Density PDF

We show the volume PDF of density (normalised by the initial value) for our different  $f_{\text{turb}}$  runs in fig. 6. For  $f_{\text{turb}} < 1.0$  we observe two peaks in the density distribution, where the denser phase corresponds to the cold phase and the rarer phase corresponds to the hot phase (see fig. 1 for projection plots). The amplitude of the cold peak



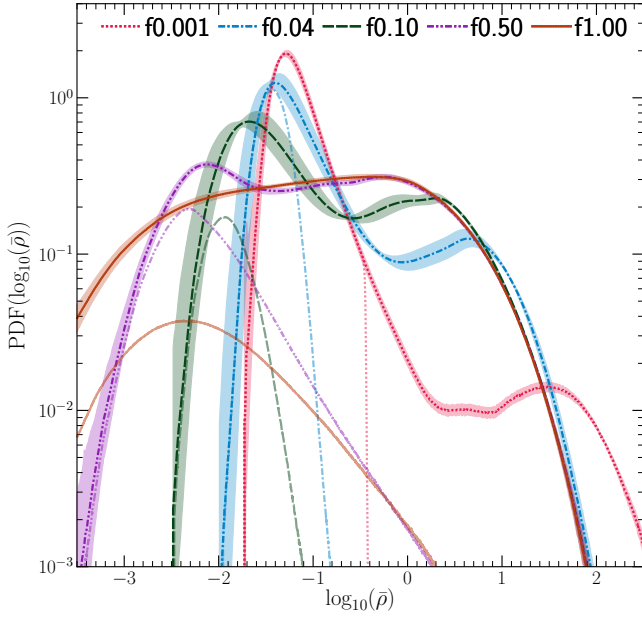


**Figure 6.** The volume PDF of the logarithm of density (normalised) of the gas for different fractions of turbulent heating. The lighter coloured lines show the PDFs of gas in the hot phase ( $T > 10^7$  K for  $f_{\text{turb}} \leq 0.10$  and  $T > 10^6$  K for  $f_{\text{turb}} > 0.10$ ). The density bimodality decreases with increasing turbulence.

increases, whereas  $\rho_{\text{cold}}$  (the value of cold phase density peak) decreases with increasing  $f_{\text{turb}}$ . This happens due to turbulent smearing of cold-phase gas—since the mass fraction of the cold phase gas is approximately similar across all runs (see first panel of fig. 2), with increasing turbulence, the cold regions are more spread out and have lower density. In other words, the dense regions are more fluffy for stronger turbulence.

The density distribution of the hot phase is also observationally important, since it represents the X-ray emitting gas in the ICM. We show these PDFs as lighter colored lines in fig. 6. The runs f0.04 and f0.10 have nearly log-normal distributions. The density distribution in all other runs (f0.001, f0.50 and f1.00) show a power-law tail at high densities. This happens because the high density gas cools faster, and its density increases as it cools, pushing it further to the right of the PDF. This shape of the PDF is also seen in the  $\gamma = 0.7$  runs in Federrath & Banerjee (2015) (see their figure 4).

### 3.3.5 Density and pressure fluctuations as a function of $\mathcal{M}_{\text{hot}}$

The density and pressure fluctuations in the hot phase gas in the ICM are used to obtain indirect estimates of turbulent gas velocities (see section 1 and Zhuravleva et al. 2014a,b; Khatri & Gaspari 2016; Simionescu et al. 2019). In fig. 7, we show the scaling of the hot phase logarithmic density (filled data points) and logarithmic pressure fluctuations (unfilled) ( $\sigma_s$  and  $\sigma_{\ln \bar{P}}$ ) with the hot phase rms Mach number ( $\mathcal{M}_{\text{hot}}$ ) for our runs with different  $f_{\text{turb}}$ . For convenience and ease of comparison, we have plotted  $\sigma_{\ln \bar{P}}/\gamma$ . We also show the  $\sigma_s, \sigma_{\ln \bar{P}}/\gamma - \mathcal{M}$  scaling relation we proposed in Mohapatra et al. (2020, 2021b) for density and pressure (here in the absence of gravitational stratification). We have used  $b = 0.33$  for solenoidal driving (see eq. 23 in Federrath et al. 2010).

We denote the total density fluctuations as  $\delta\rho_{\text{tot}}$ , and it has contributions from both turbulent density fluctuations ( $\delta\rho_{\text{turb}} = 0.33\mathcal{M}^2$

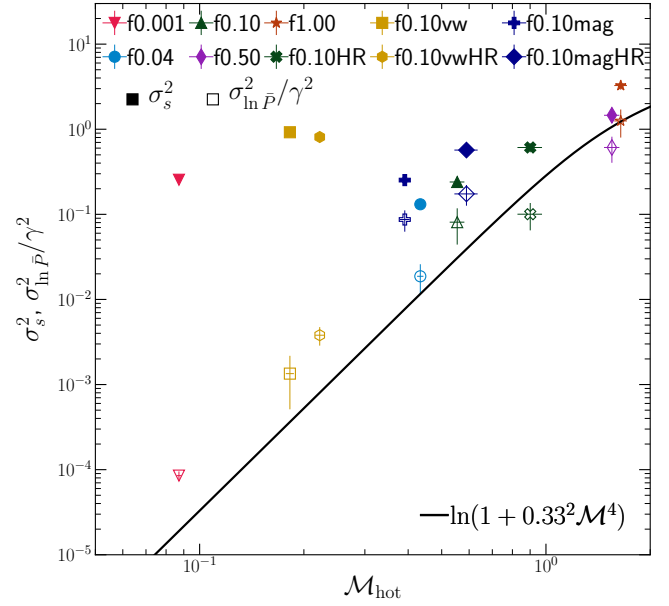


**Figure 7.** The variance of the logarithm of normalised density ( $s$ , filled) and pressure ( $\ln \bar{P}$ , unfilled) of the hot phase gas ( $T > 10^7$  K for  $f_{\text{turb}} \leq 0.10$  and  $T > 10^6$  K for  $f_{\text{turb}} > 0.10$ ) for all of our runs. The solid line shows the predicted scaling relation for subsonic turbulence with solenoidal driving and without radiative cooling (see eq. 13f in Mohapatra et al. 2021b with the Froude number  $\text{Fr} \rightarrow \infty$ ) and the driving parameter  $b = 0.33$  for solenoidal driving. Pressure fluctuations agree better with the scaling relation as compared to density fluctuations, which are much larger in the presence of radiative cooling and associated thermal instability.

for subsonic turbulence) and thermal instability ( $\delta\rho_{\text{TI}}$ ).

$$\delta\rho_{\text{tot}}^2 = \delta\rho_{\text{turb}}^2 + \delta\rho_{\text{TI}}^2 \quad (7)$$

Clearly,  $\delta\rho_{\text{TI}}^2$  (which is simply the difference between  $\delta\rho_{\text{tot}}^2$  and  $\delta\rho_{\text{turb}}^2$ ) has a much larger amplitude than  $\delta\rho_{\text{turb}}^2$  for  $f_{\text{turb}} \leq 0.5$  (subsonic turbulence). For  $f_{\text{turb}} \gtrsim 0.5$  (also when turbulence becomes supersonic),  $\delta\rho_{\text{turb}}^2$  increases in magnitude, and dominates over  $\delta\rho_{\text{TI}}^2$ .

The pressure fluctuations still follow the scaling relation with  $\mathcal{M}_{\text{hot}}$ . In Mohapatra et al. (2020, 2021b), we showed that the pressure fluctuations are unaffected by stratification as well. This makes tSZ observations a more robust method for probing turbulent velocities than X-ray brightness fluctuations. With high angular resolution SZ observations (see Mroczkowski et al. 2019 for a review), we can obtain reliable indirect estimates of turbulent velocities in the ICM.

These results are similar to the trends reported in Mohapatra & Sharma (2019), where the ‘with-cooling’ runs had larger density fluctuations than the ‘without-cooling’ runs (for the same  $\mathcal{M}_{\text{hot}}$ ), whereas the pressure fluctuations remained the same.

### 3.4 Phase diagram of density and pressure fluctuations

In this subsection, we present and discuss the joint 2D PDFs of pressure and density for three representative runs: f0.001, fiducial (f0.10) and f1.00. These phase diagrams can be used to characterise the mode of gas perturbations, which have been studied in thermal instability simulations (Das et al. 2021), mixing layer turbulence (Ji et al. 2019; Fielding et al. 2020), simulations with background stratification (Mohapatra et al. 2020) and also in X-ray observations (Zhuravleva et al. 2018). In this subsection, we discuss the role of

different levels of turbulence and the onset of thermal instability on the nature of these perturbations.

In fig. 8, we show these 2D-PDFs in two snapshots, just before (first row) and just after the formation of multiphase gas (second row). We have also shown different straight line fits which show different fluctuation modes—adiabatic, isobaric, isothermal, and isochoric (see first column in upper panel).

Before the onset of thermal instability (first row), the fluctuation modes are isobaric for f0.001 run (first column) and with increasing  $f_{\text{turb}}$ , the slope of the PDF increases and becomes adiabatic for f1.00 run. The amplitude of fluctuations is also much larger for larger  $f_{\text{turb}}$ .

For f0.001 run, only the highest density gas becomes multiphase and cools down to  $T_{\text{cutoff}}$  ( $10^4$  K). But for f0.10 and f1.00, large amplitude adiabatic modes lead to either gas with high density or lower density and lower temperature (closer to the peak of the cooling curve  $\Lambda(T)$ , see fig. 8 in Sutherland & Dopita 1993). Both of these states are prone to condensation with  $t_{\text{TI}} < t_{\text{mix}}$ . Once  $t_{\text{cool}} \ll t_{\text{cs}}$ , the gas cools isochorically, where it overlaps with the isothermal fit ( $T = T_{\text{cutoff}}$ ). The overdensity at  $\log_{10} \bar{P} \approx -2.8$  in the third column of the second row corresponds to  $P_{\text{cutoff}}$  (see eq. 5).

Fielding et al. (2020) argue that the isochoric behavior is due to lack of sufficient resolution. While this is partly true, we expect large blobs to cool isochorically through  $10^5$  K, the peak of the cooling curve (e.g., see Das et al. 2021). We present a resolution study of the 1D pressure PDFs in section 3.6.3.

Recent observations point towards the ICM being mainly dominated by isobaric modes (see fig. 6 in Zhuravleva et al. 2018). This is in line with our results—stronger turbulence leads to larger, adiabatic fluctuations whereas weaker subsonic turbulence produces mainly isobaric modes in the hot phase. In Mohapatra et al. (2020), we showed that gravitational stratification can also change the perturbation modes from adiabatic to isobaric. Our results agree with the cluster scale simulations of Gaspari & Churazov (2013). Gaspari & Churazov also showed that strong thermal conduction can introduce isothermal modes, but conduction may be suppressed in the ICM, e.g., as seen in a recent plasma experiment (Meinecke et al. 2021).

### 3.5 Tracer particles

In this subsection we present the time evolution and statistics of the Lagrangian tracer particles (see section 2.2.6). These tracers are initially uniformly distributed throughout the volume and move with the local flow. They do not have any back-reaction on the fluid.

#### 3.5.1 Evolution of particle properties

In fig. 9, we show the time evolution of  $T$  (first row),  $P$  (second row) and magnitude of velocity ( $v$ , third row) of a randomly chosen particle for three runs f0.001, fiducial (f0.10) and f1.00. All three particles are initially in the hot phase and then transition to the cold phase. Once the temperature of the particle drops, it drops all the way to  $T_{\text{cutoff}}$ , since the intermediate region is fast-cooling and short-lived. These phase changes are all associated with a drop/rise in  $P$ . We also observe that these transitions are not entirely isochoric—for example, at  $t \approx 0.2$  Gyr, for the fiducial run,  $T$  drops by 2.5 orders of magnitude, whereas  $P$  only drops by 1.5 orders, implying that the density  $\rho$  increases by an order of magnitude. The drop in  $P$  during these transitions increases with increasing  $f_{\text{turb}}$ .

There are clear drops in the particle velocities for f0.001 run during hot-cold transition and a rise in the velocity during the cold-hot transition. But for the fiducial and f1.00 runs, the stochastic turbulent

velocity changes are large and difficult to distinguish from the velocity changes, if any, associated with the phase transitions.

#### 3.5.2 Trajectory of tracers

Here we discuss the trajectories of tracer particles for our f0.001, fiducial and f1.00 runs (tracers for different runs have the same starting location). In fig. 10, we show the projected trajectories along the  $yz$  plane of five tracers, colored by their instantaneous temperature. The position and temperature of each tracer is shown every 10.4 Myr for the f0.001 run and every 1.3 Myr for the f0.10 and f1.00 runs.

The area covering fraction of projected trajectories increases with increasing  $f_{\text{turb}}$  due to higher turbulent diffusion. The particles cover larger distances due to larger turbulent velocities. For f0.001 run, we observe that many phase transitions (change in color) are also associated with jerks in the trajectory, whereas there is no noticeable effect for larger  $f_{\text{turb}}$  runs, meaning hot and cold phases may be co-moving for stronger turbulence. This has important implications for observational studies such as Li et al. (2020), where the authors measure velocities of the cold phase gas and use it to estimate velocities of the hot phase. However, note that in the presence of gravitational stratification, the cold phase may lose pressure support and move relative to the hot and roughly hydrostatic atmosphere (Wang et al. 2021).

#### 3.5.3 Probability of phase transitions

The probability of phase transitions per time ( $\dot{P}_{p_1 p_2}$  for a transition from phase  $p_1$  to  $p_2$ ) is another interesting thermodynamic statistic—it gives us information about the relative stability of different phases and the amount of mixing between them. These are motivated by the Einstein’s coefficients for transition between different energy levels of a system. We divide the gas between three phases—cold (denoted by ‘c’,  $T < 2 \times 10^4$  K), intermediate (denoted by ‘i’,  $2 \times 10^4$  K  $< T < 10^6$  K) and hot (denoted by ‘h’,  $T > 10^6$  K)<sup>4</sup>. We use a peak (and dip) detector algorithm to note changes in the temperature of the tracers, which we mark as phase changes. The quantity  $\dot{P}_{p_1 p_2}$  is defined as:

$$\dot{P}_{p_1 p_2} = \frac{N_{p_1 p_2}}{N_{p_1} t_{p_1}}, \quad (8a)$$

where  $N_{p_1 p_2}$  is the total number of transitions from phase  $p_1$  to  $p_2$ ,  $N_{p_1}$  is the total number of transitions starting from  $p_1$  ( $N_{p_1} = N_{p_1 c} + N_{p_1 i} + N_{p_1 h}$ ), and  $t_{p_1}$  is the total time spent by a particle in the phase  $p_1$ . The probability of transitioning out of the phase  $p_1$  per unit time is denoted by  $\dot{P}_{p_1}$  and is defined as:

$$\dot{P}_{p_1} = \dot{P}_{p_1 c} + \dot{P}_{p_1 i} + \dot{P}_{p_1 h} = 1/t_{p_1}, \quad \text{so} \quad (8b)$$

$$\int_0^{t_{p_1}} \dot{P}_{p_1} dt = 1. \quad (8c)$$

So a larger value of  $\dot{P}_{p_1}$  corresponds to less time spent in phase  $p_1$ , a more unstable phase. We average all these quantities over all (1000) tracers.

We have shown  $\dot{P}_{p_1 p_2}$  for all possible phase transitions in fig. 11. The transition ‘ic’ is most likely, as expected, since gas in the intermediate phase has the shortest cooling time and it cools rapidly to the cold phase. Transition from the cold phase to other phases

<sup>4</sup> Note that we define  $T_{\text{hot}} = 10^6$  K across all our runs, unlike section 3.3.5. This makes it more straightforward to compare between the different transitions probabilities as a function of  $f_{\text{turb}}$ .

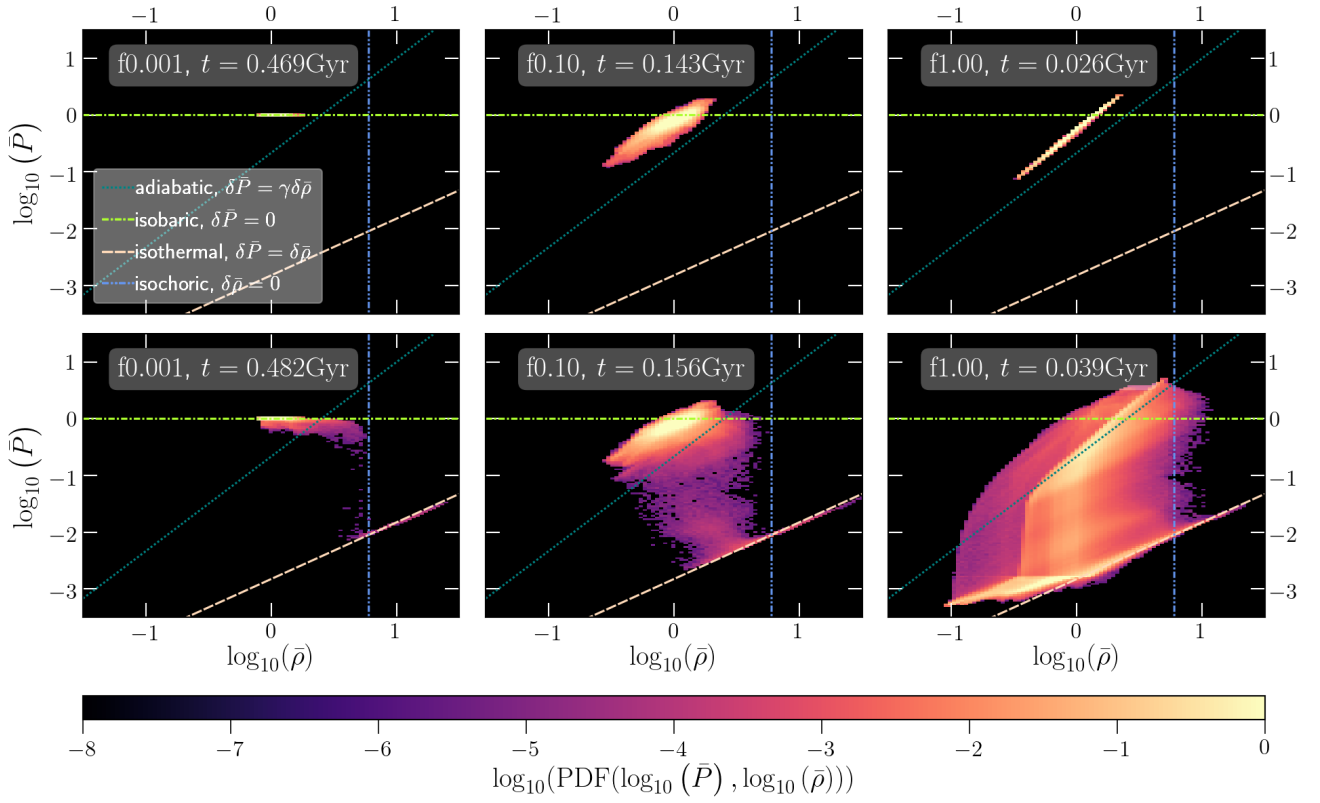


**Figure 8.** The volume PDF of the logarithm of pressure versus logarithm of density for different fractions of turbulent heating just before (first row) and after (second row) multiphase gas formation for runs with different fractions of turbulent heating. The straight lines show the different fluctuation modes—adiabatic, isobaric, isothermal, and isochoric. Before multiphase condensation, the lowest  $f_{\text{turb}}$  run is isobaric and the highest  $f_{\text{turb}}$  run is adiabatic. Notice the isochoric tracks at intermediate temperatures where  $t_{\text{cool}} \ll t_{\text{cs}}$  across the cooling blob. Also notice the overdensity on the isothermal track (the ‘peach puff’ coloured dashed line), which corresponds to  $T_{\text{cutoff}}$  at  $10^4$  K. The PDFs are broader with stronger turbulence.

‘ci’ and ‘ch’ are least likely, since particles spend most of their time in the cold phase ( $m_{\text{cold}}/m_{\text{tot}} \sim 0.7\text{--}0.9$ , see fig. 2). The rate  $\dot{P}_i$  ( $= \dot{P}_{ic} + \dot{P}_{ii} + \dot{P}_{ih} = 1/t_i$ ) decreases with increasing  $f_{\text{turb}}$ , since the amount of intermediate temperature gas increases, leading to a larger  $t_i$  (see fig. 4) due to increased turbulent mixing. The opposite trend is seen in the transition rates ‘hc’ and ‘hi’, which increase with increasing  $f_{\text{turb}}$ , as the mean temperature of the hot phase decreases, leading to a shorter cooling time. However,  $\dot{P}_{hi} \ll \dot{P}_{hc}$ , since the gas is expected to cool all the way down to the cold phase, rather than be stuck at intermediate temperatures.

### 3.6 Effects of heating model, MHD and resolution

In this subsection, we fix  $f_{\text{turb}}$  to the fiducial value (0.10) and discuss the effects of a different heating model ( $Q_{\text{vw}}$ ) and MHD. We then look at the effects of increasing resolution on these three runs.

#### 3.6.1 Effects of heating model

Here we present the effects of the heating model implemented (‘mw’ vs ‘vw’ see section 2.2.2). We compare between the fiducial f0.10 run and the f0.10vw run. The mw heating model is an idealised version of density-dependent heating mechanisms such as heating by photons and cosmic rays. The vw heating model represents energy injection into the hot phase and its subsequent mixing with the rest of the gas through turbulence. This mimics the turbulent mixing of hot AGN-inflated bubbles with the ICM.

In fig. 12, we show the  $\mathcal{M}$  (first column), temperature (second column) and pressure (third column) PDFs for these two runs. The f0.10vw run has lower Mach numbers and less gas in the intermediate phase. This happens because by construction, most of the feedback thermal heat is added to the volume-filling hot phase. This reduces the net-cooling rate, since the hotter hot phase gas cools even slower. Because the turbulent heating rate is also proportional to the net cooling rate, these simulations have weaker turbulence, inefficient mixing and less intermediate temperature gas. Due to weaker turbulent smearing, the cold phase clouds are also much smaller in size, as seen in the first row of fig. 13. In contrast, for the fiducial run, most of the thermal heat is added to the cold phase ( $m_{\text{cold}}/m_{\text{tot}} \sim 0.8$ ). This pushes the cold gas towards the fast-cooling intermediate phase, leading to an increase in the net-cooling rate and ultimately larger turbulent velocities with better mixing between the phases. The morphological features of the cold-phase gas, as well as the distribution of gas across different temperatures can be obtained from observations and be used to constrain the relative contribution from the different heating sources (for example, cosmic rays vs. turbulent mixing) towards keeping the ICM hot.

#### 3.6.2 Effect of magnetic fields

The ICM is weakly magnetized, with plasma beta  $\sim 100$  ( $\beta = 8\pi P/B \cdot B$ ) (Carilli & Taylor 2002; Govoni & Feretti 2004; Bonafede et al. 2010; Anderson et al. 2021). From Alfvén’s flux freezing theorem, the field lines are frozen into the plasma and have to move along with

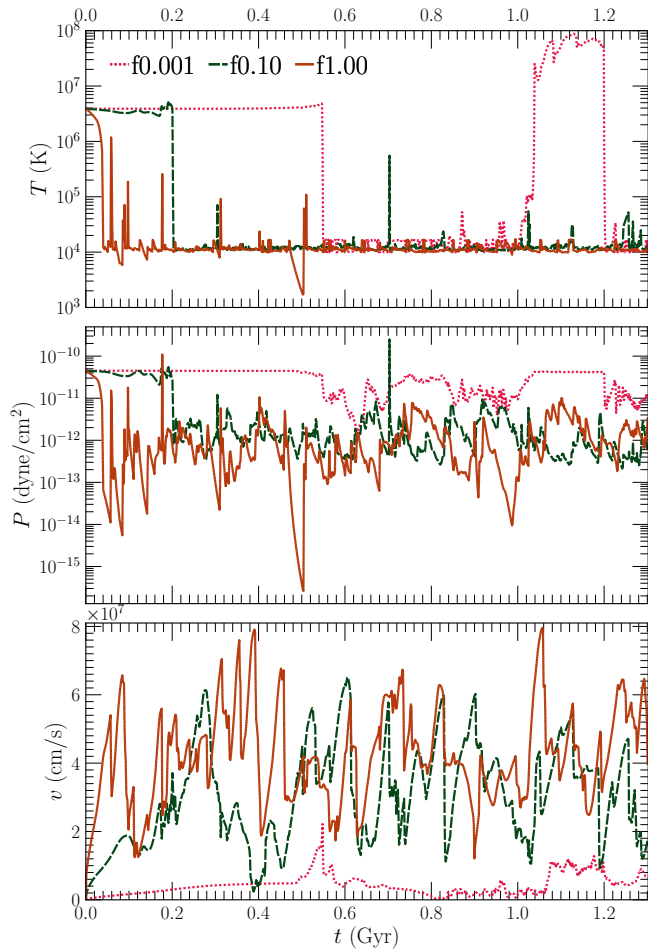


**Figure 9.** The time evolution of properties of a randomly chosen Lagrangian tracer particle: temperature (first row), pressure (second row) and magnitude of velocity (third row) for runs with different levels of turbulence. The number of excursions across phases increases with increasing  $f_{\text{turb}}$ , as expected. Velocities also increase with larger  $f_{\text{turb}}$ .

it. Hence the compressed cold phase regions formed due to thermal instability are supposed to be magnetically dominated ( $\beta < 1$ ). This also leads to their filamentary structure (Conselice et al. 2001; Fabian et al. 2008).

Magnetic fields also provide another channel of energy conversion in which turbulent kinetic energy is converted into magnetic energy. For the f0.10mag run, this leads to weaker turbulent density fluctuations and a lower cooling rate, which further decreases  $\mathcal{M}_{\text{hot}}$ , as seen in the first column of fig. 12 (refer to column 5 in table 1 for its value). Because of the lower cooling rate, the hot phase is slightly hotter (second column) and its thermal pressure is higher. The cold phase has low thermal pressure (peaking close to  $P_{\text{cutoff}}$ ), but it is partly supported by magnetic pressure. This is seen in the second and third rows of fig. 13, where the cold, dense regions and their immediate surroundings are associated with low  $\beta$  (fourth column). The higher magnetic pressure in the hot phase surrounding these cold phase regions may also contribute to larger values of  $\sigma_{\text{In}} \bar{p}$  for the MHD runs in fig. 7, as compared to predictions from the scaling relation.

### 3.6.3 Effect of resolution

Since we do not resolve  $\ell_{\text{cool}}$  (refer to section 3.1 for its definition), it is important to check the convergence of our results with resolution. In fig. 12, we observe that on doubling the resolution (from  $384^3$  to  $768^3$ ), there is a slight increase in the hot phase Mach number (first column, low Mach number peak). The temperature (second column) PDFs also show more gas at intermediate temperatures and a lower temperature of the hot phase. In the pressure PDFs (third column), we find more gas at intermediate pressures between the two peaks corresponding to the phases. The hot phase peak is also at a slightly lower value. Most of these changes can be explained by an increase in the cooling rate, which leads to an increase in the strength of turbulence due to the energy balance condition in our setup. This leads to more mixing between the hot and cold phases and further decreases the temperature of the hot phase and transfers more gas into the intermediate phase.

Mandelker et al. (2021) also find the cold gas mass fraction to increase with increasing resolution in their study of the multi-phase intergalactic medium. They argue that in simulations that do not resolve  $\ell_{\text{cool}}$ , the gas piles up near  $T \sim 10^5$  K (corresponding to the peak of the cooling curve) and cooling to lower temperatures becomes inefficient. This is in agreement with our results. Fielding et al. (2020) show that upon increasing resolution, the bimodal distribution in pressure disappears for a radiative shear layer. Their highest resolution PDFs converge with the hot and cold phases in rough pressure equilibrium (see their fig. 5). However, Dutta et al. (2021) have found analytic cooling flow solutions around cold clouds that are sustained by mild pressure gradients between the ambient hot gas and the cold cloud. We find that our hot- and cold-phase pressure peaks move closer to each other upon increasing resolution, but this could partly be due to the increased strength of turbulent mixing (due to the larger cooling rate) in the higher-resolution runs.

Comparing the projection plots in the second and third rows of fig. 13, we observe that the cold clouds have smaller physical size for the higher resolution run. This can be seen quite clearly in the cold gas emission plot in the third column. These clouds are expected to become even smaller as we further increase resolution and reach convergence once the grid resolves important length scales. In addition to this, numerical diffusion is expected to affect the statistical properties of turbulence for scales  $\ell \lesssim 30\Delta x$  (Kitsionas et al. 2009; Federrath et al. 2010, 2011)<sup>5</sup>. Hence the condition for numerical convergence becomes:  $\Delta x \lesssim \min(\ell_{\text{cool}}, \ell_{\text{Field}}, \ell_{\nu})/30$ , where  $\ell_{\text{Field}} = \sqrt{D t_{\text{cool}}}$  corresponds to the scale where the thermal conduction time is equal to  $t_{\text{cool}}$ ,  $D$  being the explicit diffusion constant (Koyama & Inutsuka 2004; Sharma et al. 2010). However, both  $\ell_{\text{Field}}$  and  $\ell_{\nu}$  (the viscous length scale) are suppressed in the hot ICM (Roberg-Clark et al. 2018; Zhuravleva et al. 2019), giving us even more stringent resolution requirements to get convergence for physical parameters. The scale  $\ell_{\nu}$  is also suppressed in the cold phase (Li et al. 2020).

## 4 CAVEATS AND FUTURE WORK

In this section, we discuss some of the shortcomings of our study and future prospects of our work.

<sup>5</sup> Note that the power injected by driving turbulence may also leak to scales smaller than  $L/2$ , since the turbulent forcing power ( $\rho v^3/\ell$ ) is coupled to the small-scale density variations (Grete et al. 2017) in our multi-phase setup. This effect can further reduce the dynamical range of turbulence, since driving would affect statistics on scales smaller than  $L/2$ .

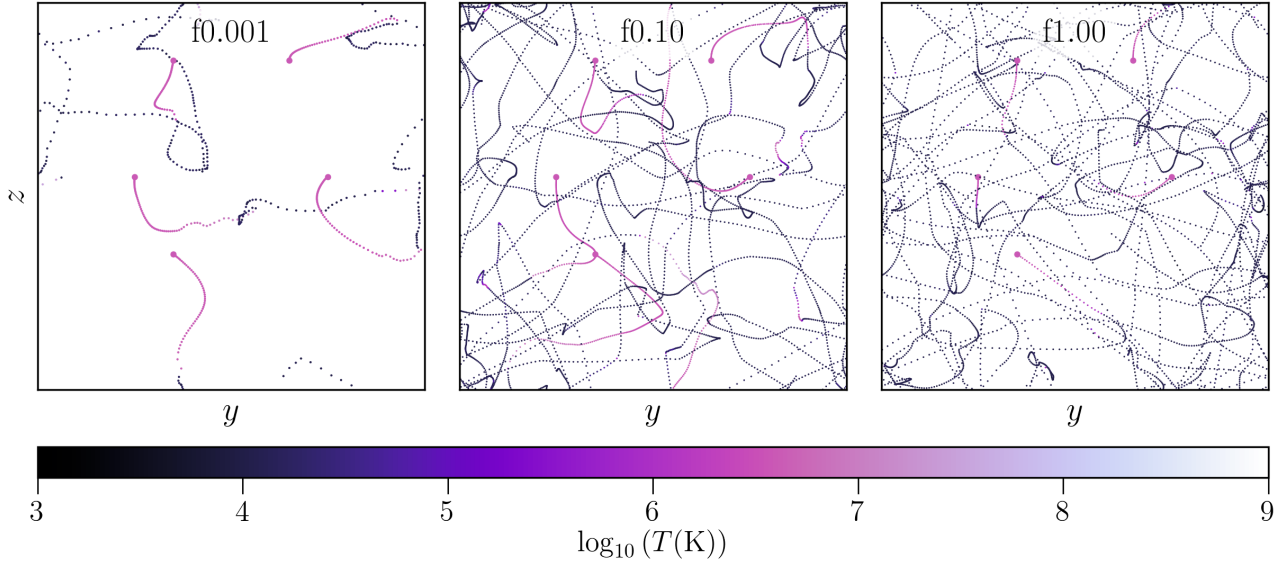


**Figure 10.** The projected trajectory in the  $yz$ -plane of five randomly chosen tracer particles with same starting location over the entire duration of our simulations (1.302 Gyr). The three panels are for our three representative simulations: f0.001, f0.10 and f1.00. The color represents the temperature of the tracer particle. The initial position of the particle is denoted by a large pink dot. The subsequent scatter points are 10.4 Myr apart for f0.001 and 1.3 Myr apart for runs f0.10 and f1.00. The runs with higher turbulence have much larger diffusion of the tracer particles, as seen by a larger coverage of the  $yz$  plane.

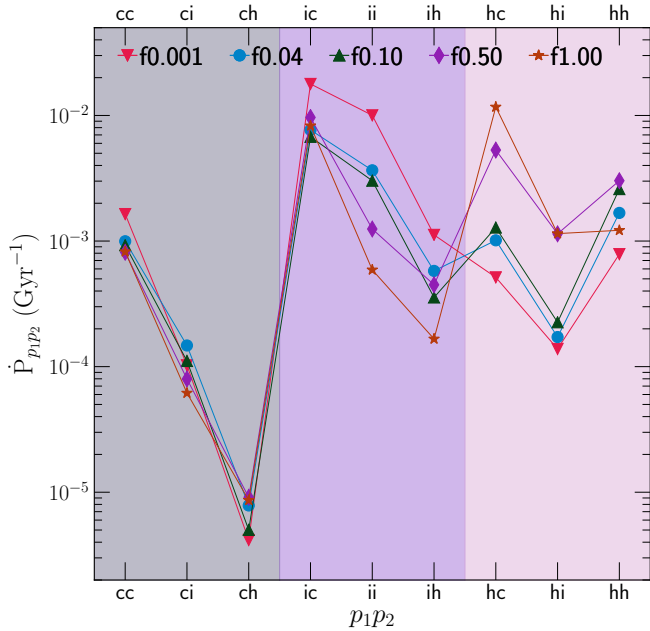


**Figure 11.** A scatter plot of transition probability per unit time of particles from phase  $p_1$  to  $p_2$  (denoted by  $\dot{P}_{p_1 p_2}$ ). The background colour represents the phase  $p_1$ —grey, purple and pink for cold, intermediate and hot phases, respectively. Among the three phases, the particles are most likely to transition into the cold phase, and most likely to transition out of the intermediate phase. There are also clear trends with  $f_{\text{turb}}$ , which we discuss in the main text.

The ICM is known to be stratified due to the gravitational potential set by the dark matter halo. However, we have ignored the effects of stratification in this set of idealised simulations. Density fluctuations in stratified turbulence are supposed to be much stronger (Mohapatra et al. 2020, 2021b) and comparable to the magnitudes seen in fig. 7.

They can also influence the mode of density perturbations in the ICM, changing them from adiabatic to isobaric. The dense cold-phase gas in our simulations would fall in the presence of gravity, as seen in Wang et al. (2021). Our runs with low  $f_{\text{turb}}$  produce a somewhat hotter hot phase. But in the presence of stratification, this thermally heated gas can rise against the density gradient, expand and cool adiabatically. The ratio between the cooling time and the free-fall time is known to play an important role in thermal instability in these environments (Sharma et al. 2012; Choudhury & Sharma 2016; Choudhury et al. 2019; Voit 2021). We plan to include stratification and study its effects in a future thermal instability study.

In order to directly focus on the impact of different levels of turbulent heating, we fixed our initial conditions (density and temperature) across all simulations. While the different levels of turbulent to thermal pressure ratio can represent the gas in halos of different masses (lower mass halos being more turbulent), our initial conditions are more applicable to cool and thermally unstable regions in groups and clusters.

We have conducted two MHD simulations, with fixed initial magnetic field geometry. We have studied their effects on the gas distribution across different temperatures, densities and pressure. However, our results could be sensitive to the choice of the initial field configuration and its initial amplitude, which are not well-constrained from observations. We plan to investigate these effects in a follow-up study focusing on the effects of the magnetic field geometry, amplitude and orientation, on the structure and distribution of the multi-phase gas.

In order to make accurate predictions of different observables at different temperatures, such as the column densities of HI, MgII, CIV, OVI, FeXXVI, etc., we need to track these species through chemical networks, non-equilibrium ionisation and photoionisation modelling. However, these methods are computationally expensive and have not been included in this study.

We have not included thermal conduction in our simulations. Thermal conduction is supposed to be suppressed and anisotropic in the ICM plasma (Roberg-Clark et al. 2016; Meinecke et al. 2021). But

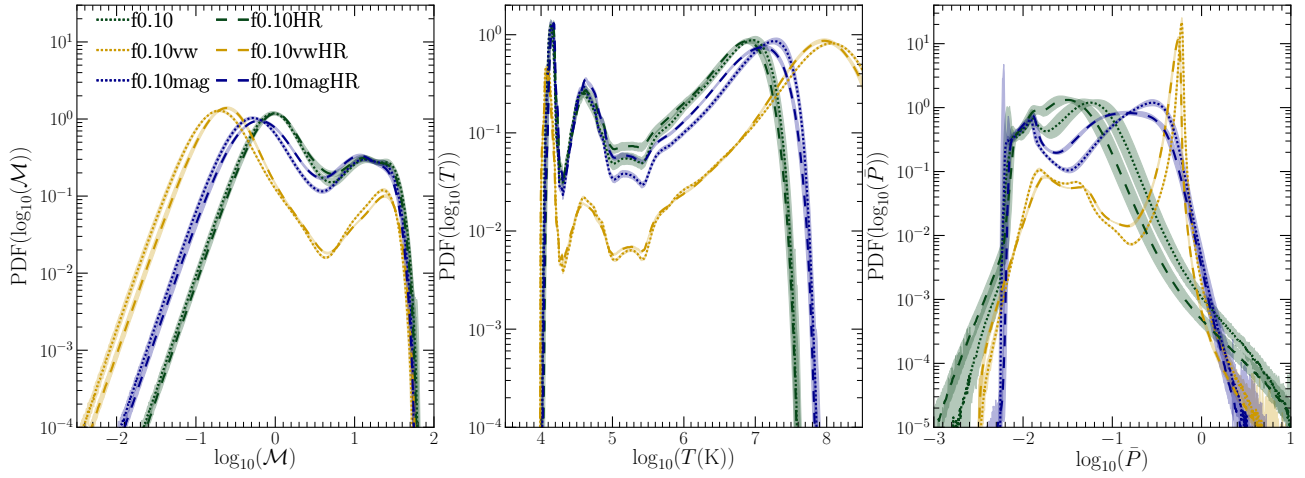


**Figure 12.** The volume-weighted PDFs of the logarithms of  $\mathcal{M}$  (first column), temperature (second column) and pressure (third column) for runs with different heating models, MHD runs and higher resolution runs (dashed lines). Both magnetic fields and ‘vw’ thermal heating lead to weaker turbulence. All the PDFs are averaged over 28 snapshots from  $t = 0.651$  Gyr to  $t = 1.003$  Gyr.

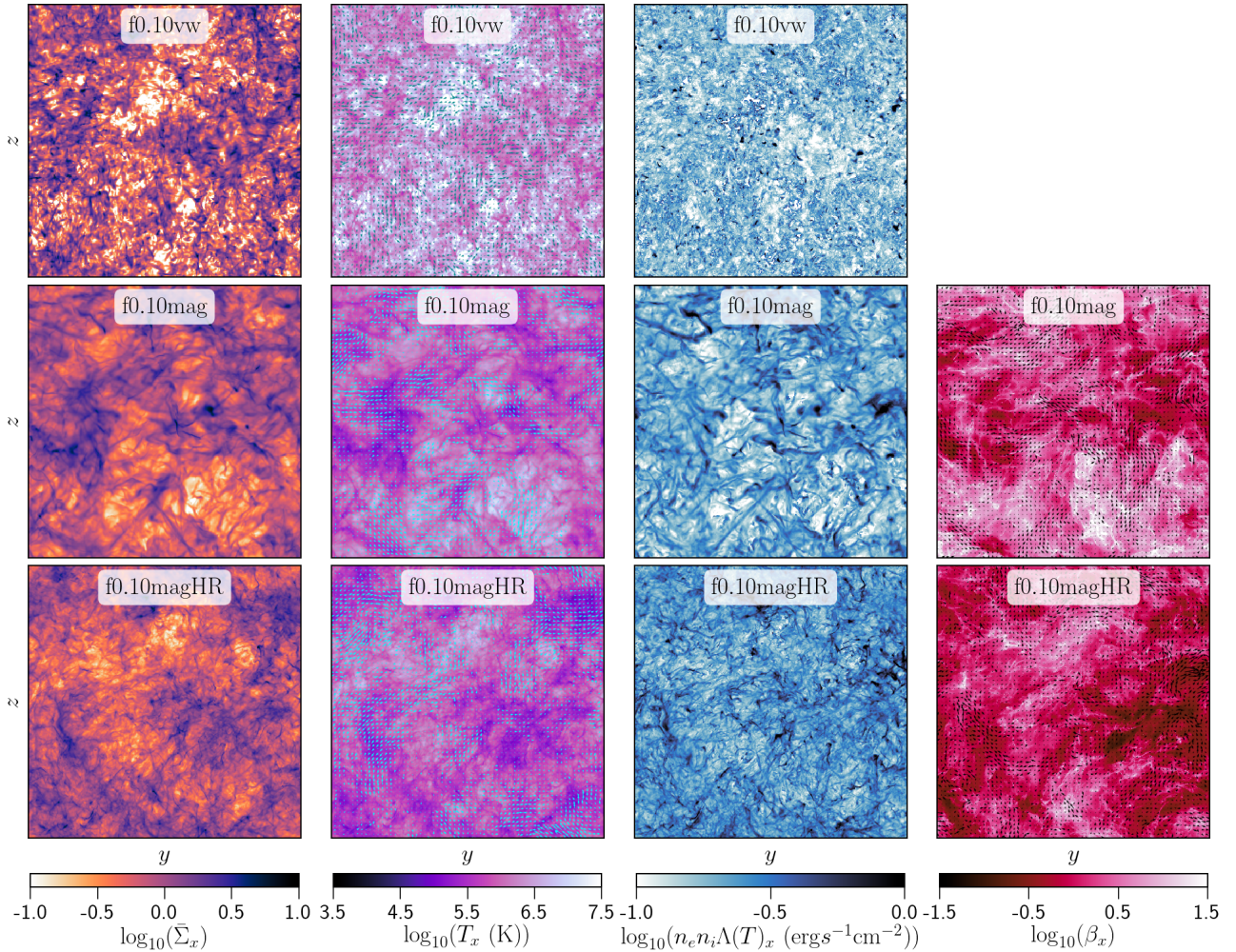


**Figure 13.** First three columns: same as fig. 1, but for runs f0.10vw, f0.10mag and f0.10magHR at  $t = 0.911$  Gyr. The colorbar scale for column 3 has been adjusted. Fourth column: The volume-weighted projection of plasma beta, the ratio of thermal to magnetic pressure in log scale. The black arrows represent the projected  $\mathbf{B}$  perpendicular to the LOS. The f0.10vw run has more small scale cold gas due to weaker turbulence. For the runs with magnetic fields, regions of low plasma beta are associated with gas in the cold phase. With increasing resolution, the size of the cold gas clumps becomes smaller.

as shown in [Gaspari & Churazov \(2013\)](#), it can wipe out small scale structures even when suppressed by a factor of  $\sim 10$  relative to the Spitzer value. It can also populate gas at intermediate temperatures and introduce isothermal modes of perturbation.

Our local ICM boxes only have a resolution of  $\approx 100\text{--}50$  pc for our standard and high resolution runs. We require much higher spatial resolution to resolve mixing layers in the multiphase gas ([Fielding et al. 2020](#)). The scale separation between the two phases may also be much more than what we observe in this study – we observe that the size of cold clouds decreases on increasing resolution.

## 5 CONCLUSIONS

In this study we have focused on the effects of different fractions of turbulent heating in an energetically balanced simulation of the ICM. Here we summarise some of the main takeaway points of our work:

(i) Turbulence seeds thermal instability in the hot phase gas, which separates into hot and cold phases. These phases are distinguishable as separate peaks in the Mach number, temperature, pressure and density PDFs. Most of the mass of the gas is in the cold phase but the hot phase occupies most of the volume.

(ii) Mixing due to turbulence increases the fraction of gas at the thermally unstable intermediate regions near the peak of the cooling curve ( $T \sim 10^{5.5}$  K).

(iii) The density fluctuations in the thermally unstable hot phase gas are much larger than the fluctuations predicted by  $\sigma_s\text{--}\mathcal{M}$  scaling relations based on homogeneous idealised turbulence. But the pressure fluctuations in the hot phase are unaffected by thermal instability and they obey the same scaling relations.

(iv) The mode of density fluctuations in the hot phase changes from isobaric to adiabatic for stronger turbulence. The phase transition from the hot phase to the cold phase during condensation is mostly isochoric. The fluctuations in the cold phase are isothermal at the cooling-cutoff temperature.

(v) The intermediate temperature phase gas is the most unstable gas phase, but its stability increases with increasing turbulent velocities.

(vi) Using different heating prescriptions (volume-weighted vs mass-weighted) can affect the amount of gas in the two phases. The volume-weighted prescription deposits more feedback heat in the hot volume-filling phase.

(vii) In MHD runs, turbulent kinetic energy is converted into magnetic energy, which leads to lower turbulent velocities. The gas in the cold phase is at low thermal pressure and is dominated by magnetic pressure.

## ACKNOWLEDGEMENTS

This work was carried out during the ongoing COVID-19 pandemic. The authors would like to acknowledge the health workers all over the world for their role in fighting in the frontline of this crisis. The authors would like to thank Dr. Philipp Grete for a constructive referee report, which helped to improve this work. RM thanks Prof. Naomi M. McClure-Griffiths for organising a writing retreat, where a part of this work was written. CF acknowledges funding provided by the Australian Research Council (Future Fellowship FT180100495), and the Australia-Germany Joint Research Cooperation Scheme (UA-DAAD). PS acknowledges a Swarnajayanti Fellowship (DST/SJF/PSA-03/2016-17) and a National Supercomputing

Mission (NSM) grant from the Department of Science and Technology, India. We further acknowledge high-performance computing resources provided by the Leibniz Rechenzentrum and the Gauss Centre for Supercomputing (grants pr32lo, pr48pi and GCS Large-scale project 10391), the Australian National Computational Infrastructure (grant ek9) in the framework of the National Computational Merit Allocation Scheme and the ANU Merit Allocation Scheme. The simulation software FLASH was in part developed by the DOE-supported Flash Center for Computational Science at the University of Chicago.

## 6 DATA AVAILABILITY

All the relevant data associated with this article is available upon request to the corresponding author.

## 7 ADDITIONAL LINKS

Movies of projected density and temperature of different simulations are available as online supplementary material, as well as at the following links on youtube:

- (i) [Movie](#) of the fiducial simulation.
- (ii) [Movie](#) of the f0.10HR simulation.
- (iii) [Movie](#) of the f0.10vHR simulation.
- (iv) [Movie](#) of the f0.10magHR simulation.

We also show a [movie](#) of fig. 8 and a [movie](#) of tracer particles.

## 8 SOFTWARE USED

We have used the following software and packages for our work: FLASH ([Fryxell et al. 2000](#); [Dubey et al. 2008](#)), matplotlib ([Hunter 2007](#)), cmasher ([van der Velden 2020](#)), scipy ([Virtanen et al. 2020](#)), NumPy ([Harris et al. 2020](#)), h5py ([Collette 2013](#)) and astropy ([Astropy Collaboration et al. 2018](#)).

## REFERENCES

- Anderson M. E., Sunyaev R., 2016, *MNRAS*, **459**, 2806  
 Anderson M. E., Sunyaev R., 2018, *A&A*, **617**, A123  
 Anderson C. S., et al., 2021, *Publ. Astron. Soc. Australia*, **38**, e020  
 Antolin P., 2020, *Plasma Physics and Controlled Fusion*, **62**, 014016  
 Armillotta L., Fraternali F., Marinacci F., 2016, *MNRAS*, **462**, 4157  
 Aronovitz J. A., Nelson D. R., 1984, *Phys. Rev. A*, **29**, 2012  
 Astropy Collaboration et al., 2018, *AJ*, **156**, 123  
 Audit E., Hennebelle P., 2005, *A&A*, **433**, 1  
 Balbus S. A., Soker N., 1990, *ApJ*, **357**, 353  
 Banda-Barragán W. E., Parkin E. R., Federrath C., Crocker R. M., Bicknell G. V., 2016, *MNRAS*, **455**, 1309  
 Banerjee N., Sharma P., 2014, *MNRAS*, **443**, 687  
 Bauer A., Springel V., 2012, *MNRAS*, **423**, 2558  
 Begelman M. C., Fabian A. C., 1990, *MNRAS*, **244**, 26P  
 Böhringer H., Werner N., 2010, *A&ARv*, **18**, 127  
 Bonafede A., Ferretti L., Murgia M., Govoni F., Giovannini G., Dallacasa D., Dolag K., Taylor G. B., 2010, *A&A*, **513**, A30  
 Bordoloi R., et al., 2017, *ApJ*, **834**, 191  
 Boselli A., et al., 2019, *A&A*, **623**, A52  
 Bouchut F., Klingenberg C., Waagan K., 2007, *Numerische Mathematik*, **108**, 7  
 Bouchut F., Klingenberg C., Waagan K., 2010, *Numerische Mathematik*, **115**, 647

- Bray K. N. C., Cant R. S., 1991, *Proceedings of the Royal Society of London Series A*, **434**, 217
- Bregman J. N., Fabian A. C., Miller E. D., Irwin J. A., 2006a, *ApJ*, **642**, 746
- Bregman J. N., Otte B., Miller E. D., Irwin J. A., 2006b, *ApJ*, **642**, 759
- Carilli C. L., Taylor G. B., 2002, *ARA&A*, **40**, 319
- Choudhury P. P., Sharma P., 2016, *MNRAS*, **457**, 2554
- Choudhury P. P., Sharma P., Quataert E., 2019, *MNRAS*, **488**, 3195
- Churazov E., Sunyaev R., Forman W., Böhringer H., 2002, *MNRAS*, **332**, 729
- Churazov E., Forman W., Jones C., Böhringer H., 2003, *ApJ*, **590**, 225
- Collette A., 2013, Python and HDF5. O'Reilly
- Conselice C. J., Gallagher John S. I., Wyse R. F. G., 2001, *AJ*, **122**, 2281
- Creasey P., Theuns T., Bower R. G., Lacey C. G., 2011, *MNRAS*, **415**, 3706
- Das H. K., Choudhury P. P., Sharma P., 2021, *MNRAS*, **502**, 4935
- Di Teodoro E. M., McClure-Griffiths N. M., Lockman F. J., Armillotta L., 2020, *Nature*, **584**, 364
- Dubey A., et al., 2008, in Pogorelov N. V., Audit E., Zank G. P., eds, *Astronomical Society of the Pacific Conference Series Vol. 385, Numerical Modeling of Space Plasma Flows*. p. 145
- Dutta A., Sharma P., Nelson D., 2021, arXiv e-prints, p. arXiv:2107.02722
- Edge A. C., 2001, *MNRAS*, **328**, 762
- Eswaran V., Pope S. B., 1988, *Computers and Fluids*, **16**, 257
- Fabian A. C., Sanders J. S., Taylor G. B., Allen S. W., Crawford C. S., Johnstone R. M., Iwasawa K., 2006, *MNRAS*, **366**, 417
- Fabian A. C., Johnstone R. M., Sanders J. S., Conselice C. J., Crawford C. S., Gallagher J. S. I., Zweibel E., 2008, *Nature*, **454**, 968
- Federrath C., Banerjee S., 2015, *MNRAS*, **448**, 3297
- Federrath C., Roman-Duval J., Klessen R. S., Schmidt W., Mac Low M. M., 2010, *A&A*, **512**, A81
- Federrath C., Sur S., Schleicher D. R. G., Banerjee R., Klessen R. S., 2011, *ApJ*, **731**, 62
- Field G. B., 1965, *ApJ*, **142**, 531
- Fielding D. B., Ostriker E. C., Bryan G. L., Jermyn A. S., 2020, *ApJ*, **894**, L24
- Foullon C., Verwichte E., Nakariakov V. M., Nykyri K., Farrugia C. J., 2011, *ApJ*, **729**, L8
- Foullon C., Verwichte E., Nykyri K., Aschwanden M. J., Hannah I. G., 2013, *ApJ*, **767**, 170
- Fox A. J., et al., 2015, *ApJ*, **799**, L7
- Fromang S., Papaloizou J., 2007, *A&A*, **476**, 1113
- Fryxell B., et al., 2000, *The Astrophysical Journal Supplement Series*, **131**, 273
- Gaspari M., Churazov E., 2013, *A&A*, **559**, A78
- Gendron-Marsolais M., et al., 2018, *MNRAS*, **479**, L28
- Glover S. C. O., Federrath C., Mac Low M. M., Klessen R. S., 2010, *MNRAS*, **404**, 2
- Govoni F., Feretti L., 2004, *International Journal of Modern Physics D*, **13**, 1549
- Grete P., O'Shea B. W., Beckwith K., Schmidt W., Christlieb A., 2017, *Physics of Plasmas*, **24**, 092311
- Grete P., O'Shea B. W., Beckwith K., 2020, *ApJ*, **889**, 19
- Gronke M., Oh S. P., 2018, *MNRAS*, **480**, L111
- Harris C. R., et al., 2020, Array programming with NumPy (arXiv:2006.10256), doi:10.1038/s41586-020-2649-2, <https://doi.org/10.1038/s41586-020-2649-2>
- Hennebelle P., Audit E., 2007, *A&A*, **465**, 431
- Hillel S., Soker N., 2020, *ApJ*, **896**, 104
- Hitomi Collaboration 2016, *Nature*, **535**, 117
- Hu E. M., 1992, *ApJ*, **391**, 608
- Hunter J. D., 2007, *Computing in Science Engineering*, **9**, 90
- Ji S., Oh S. P., Masterson P., 2019, *MNRAS*, **487**, 737
- Kanjilal V., Dutta A., Sharma P., 2021, *MNRAS*, **501**, 1143
- Kazantsev A. P., 1968, *Soviet Journal of Experimental and Theoretical Physics*, **26**, 1031
- Khatri R., Gaspari M., 2016, *MNRAS*, **463**, 655
- Kitsionas S., et al., 2009, *A&A*, **508**, 541
- Kolmogorov A. N., 1941, *Akademia Nauk SSSR Doklady*, **32**, 16
- Koyama H., Inutsuka S.-i., 2004, *ApJ*, **602**, L25
- Li Y., et al., 2020, *ApJ*, **889**, L1
- Mandelker N., van den Bosch F. C., Springel V., van de Voort F., Burchett J. N., Butsky I. S., Nagai D., Oh S. P., 2021, arXiv e-prints, p. arXiv:2107.03395
- Marchal A., Martin P. G., Gong M., 2021, arXiv e-prints, p. arXiv:2106.12683
- Marder B., 1987, *Journal of Computational Physics*, **68**, 48
- McCourt M., Sharma P., Quataert E., Parrish I. J., 2012, *MNRAS*, **419**, 3319
- McDonald M., Veilleux S., Rupke D. S. N., 2012, *ApJ*, **746**, 153
- Meinecke J., et al., 2021, arXiv e-prints, p. arXiv:2105.08461
- Mitran S. M., 2009, in Pogorelov N. V., Audit E., Colella P., Zank G. P., eds, *Astronomical Society of the Pacific Conference Series Vol. 406, Numerical Modeling of Space Plasma Flows: ASTRONUM-2008*. p. 249
- Mohapatra R., Sharma P., 2019, *MNRAS*, **484**, 4881
- Mohapatra R., Federrath C., Sharma P., 2020, *MNRAS*, **493**, 5838
- Mohapatra R., Jetli M., Sharma P., Federrath C., 2021a, arXiv e-prints, p. arXiv:2109.01771
- Mohapatra R., Federrath C., Sharma P., 2021b, *MNRAS*, **500**, 5072
- Mroczkowski T., et al., 2019, *Space Sci. Rev.*, **215**, 17
- Nelson K., Rudd D. H., Shaw L., Nagai D., 2012, *ApJ*, **751**, 121
- Nelson D., et al., 2020, *MNRAS*, **498**, 2391
- Olivares V., et al., 2019, *A&A*, **631**, A22
- Omma H., Binney J., Bryan G., Slyz A., 2004, *MNRAS*, **348**, 1105
- Oppenheimer B. D., 2018, *MNRAS*, **480**, 2963
- Pal N., Perlekar P., Gupta A., Pandit R., 2016, *Phys. Rev. E*, **93**, 063115
- Peterson J. R., Fabian A. C., 2006, *Phys. Rep.*, **427**, 1
- Roberg-Clark G. T., Drake J. F., Reynolds C. S., Swisdak M., 2016, *ApJ*, **830**, L9
- Roberg-Clark G. T., Drake J. F., Reynolds C. S., Swisdak M., 2018, *Phys. Rev. Lett.*, **120**, 035101
- Rose T., et al., 2019, *MNRAS*, **489**, 349
- Schmidt W., Hillebrandt W., Niemeyer J. C., 2006, *Computers & Fluids*, **35**, 353
- Sharma P., Parrish I. J., Quataert E., 2010, *ApJ*, **720**, 652
- Sharma P., McCourt M., Quataert E., Parrish I. J., 2012, *MNRAS*, **420**, 3174
- Simionescu A., et al., 2019, *Space Sci. Rev.*, **215**, 24
- Slavin J. D., Shull J. M., Begelman M. C., 1993, *ApJ*, **407**, 83
- Sparks W. B., Donahue M., Jordán A., Ferrarese L., Côté P., 2004, *ApJ*, **607**, 294
- Sunyaev R. A., Zeldovich Y. B., 1970, *Ap&SS*, **7**, 3
- Sutherland R. S., Dopita M. A., 1993, *The Astrophysical Journal Supplement Series*, **88**, 253
- Tan B., Oh S. P., Gronke M., 2021, *MNRAS*, **502**, 3179
- Tremblay G. R., et al., 2018, *ApJ*, **865**, 13
- Tumlinson J., et al., 2011, *Science*, **334**, 948
- Tumlinson J., Peebles M. S., Werk J. K., 2017, *Annual Review of Astronomy and Astrophysics*, **55**, 389
- Van Leer B., 1984, *SIAM Journal on Scientific and Statistical Computing*, **5**, 1
- Vantyghem A. N., et al., 2019, *ApJ*, **870**, 57
- Vantyghem A. N., et al., 2021, *ApJ*, **910**, 53
- Vázquez-Semadeni E., Gazol A., Scalo J., 2000, *ApJ*, **540**, 271
- Virtanen P., et al., 2020, *Nature Methods*, **17**, 261
- Voit G. M., 2021, *ApJ*, **908**, L16
- Waagan K., 2009, *Journal of Computational Physics*, **228**, 8609
- Waagan K., Federrath C., Klingenberg C., 2011, *Journal of Computational Physics*, **230**, 3331
- Wang C., Ruzsowski M., Pfrommer C., Oh S. P., Yang H. Y. K., 2021, *MNRAS*, **504**, 898
- Werk J. K., et al., 2014, *ApJ*, **792**, 8
- Werner N., et al., 2013, *ApJ*, **767**, 153
- Werner N., et al., 2014, *MNRAS*, **439**, 2291
- Wittor D., Gaspari M., 2020, *MNRAS*, **498**, 4983
- Wolfire M. G., Hollenbach D., McKee C. F., Tielens A. G. G. M., Bakes E. L. O., 1995a, *ApJ*, **443**, 152
- Wolfire M. G., McKee C. F., Hollenbach D., Tielens A. G. G. M., 1995b, *ApJ*, **453**, 673
- Zeldovich Y. B., Sunyaev R. A., 1969, *Ap&SS*, **4**, 301
- Zhuravleva I., et al., 2014a, *Nature*, **515**, 85
- Zhuravleva I., et al., 2014b, *ApJ*, **788**, L13



Zhuravleva I., Allen S. W., Mantz A., Werner N., 2018, [ApJ](#), **865**, 53  
Zhuravleva I., Churazov E., Schekochihin A. A., Allen S. W., Vikhlinin A.,  
Werner N., 2019, [Nature Astronomy](#), **3**, 832  
van der Velden E., 2020, [The Journal of Open Source Software](#), **5**, 2004

This paper has been typeset from a  $\text{\TeX/L\AA\TeX}$  file prepared by the author.